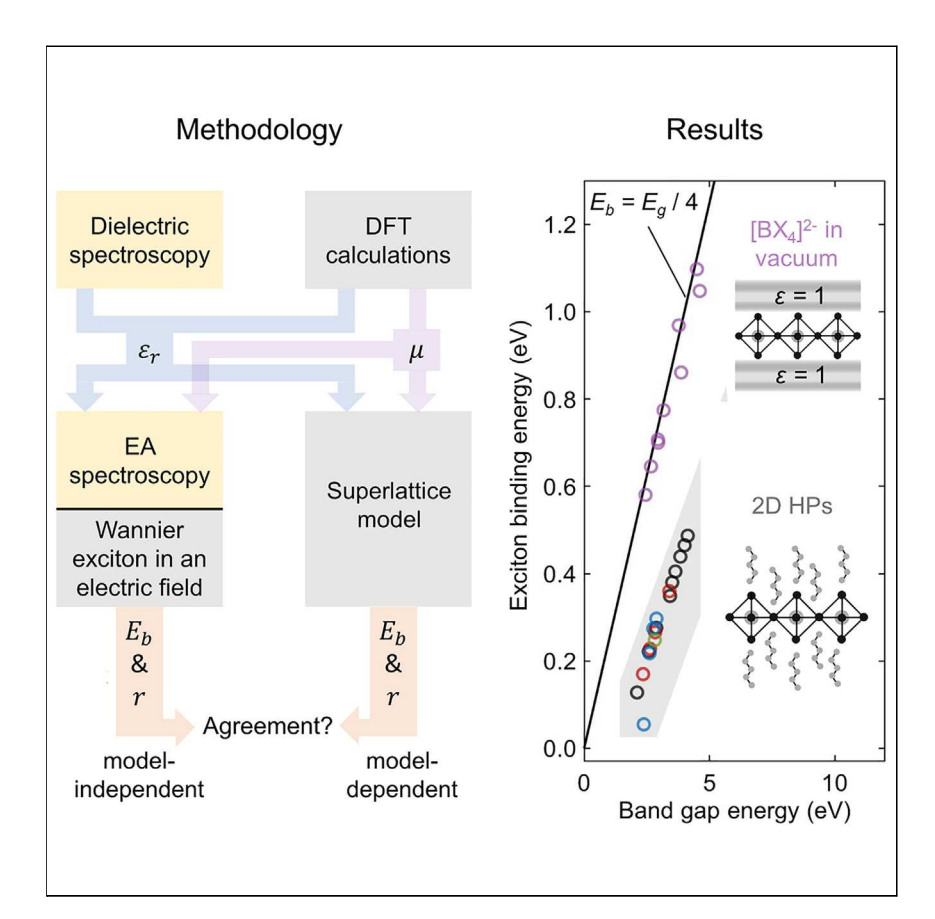
**Matter** 



## **Article**

# Mechanistic origins of excitonic properties in 2D perovskites: Implications for exciton engineering



Exciton properties dictate the optical and electronic behavior of low-dimensional semiconductors; however, these properties have remained uncertain for 2D perovskites because of conflicting reports. This study uses spectroscopic tools to precisely measure exciton properties and theory to understand the observed trends. The reduced noise floor of our measurements renders clear a correlation between the band-gap energy and exciton binding energy. Thus, traditional "band-gap engineering" also affects the strength of Coulomb interactions. Understanding these correlations allows more informed engineering of low-dimensional semiconductors.

3 Understanding
Dependency and conditional studies on material behavior

Kameron R. Hansen, Cindy Y. Wong, C. Emma McClure, ..., André Schleife, John S. Colton, Luisa Whittaker-Brooks

kameron.hansen@utah.edu

#### Highlights

Direct measurements of  $E_b$  for 31 unique perovskite structures

A strong correlation between  $E_b$  and  $E_g$  is identified and shown to be useful

We find that a superlattice model accurately describes the exciton properties

Dielectric constants and theory show that excitons are partially screened by phonons

Hansen et al., Matter 6, 3463–3482 October 4, 2023 © 2023 Elsevier Inc. https://doi.org/10.1016/j.matt.2023.07.004



## **Matter**



#### **Article**

## Mechanistic origins of excitonic properties in 2D perovskites: Implications for exciton engineering

Kameron R. Hansen, <sup>1,7,\*</sup> Cindy Y. Wong, <sup>2,6</sup> C. Emma McClure, <sup>3,4,6</sup> Blake Romrell, <sup>3</sup> Laura Flannery, <sup>2</sup> Daniel Powell, <sup>1</sup> Kelsey Garden, <sup>1</sup> Alex Berzansky, <sup>1</sup> Michele Eggleston, <sup>3</sup> Daniel J. King, <sup>3</sup> Carter M. Shirley, <sup>3</sup> Matthew C. Beard, <sup>4</sup> Wanyi Nie, <sup>5</sup> André Schleife, <sup>2</sup> John S. Colton, <sup>3</sup> and Luisa Whittaker-Brooks <sup>1</sup>

#### **SUMMARY**

As the field of 2D halide perovskites (HPs) matures, state-of-the-art techniques to measure important properties, such as the band gap  $(E_g)$  and exciton binding energy  $(E_b)$ , continue to produce inconsistent values. Here, we tackle this long-standing problem by obtaining direct measurements of  $E_g$  and  $E_b$  for 31 unique HP structures. The  $E_b$  values are lower than in previous literature reports and lower than expected from standard theory that assumes excitons are screened by optical-frequency dielectric constants. These low  $E_b$  values are shown to be a consequence of unique screening effects, such as superlattice screening and phonon screening. We find a strikingly strong correlation between  $E_b$  and  $E_g$  and provide design principles to a priori tune  $E_g$  and  $E_b$  to their optimal values. As such, this work offers a blueprint for  $E_g$ - $E_b$  engineering of low-dimensional semiconductors as an even more useful replacement for simply band-gap engineering.

#### **INTRODUCTION**

Coulomb interactions govern most optoelectronic properties in semiconductors, including band gap, excitons, polaron formation, light absorption, interaction of carriers with defects, charge, and energy transport. A clear signature of the strength of many-body Coulomb interactions is the exciton binding energy ( $E_b$ ), and precise measurements of  $E_b$  are a great driving force in advancing the understanding of and control over semiconductors. This is particularly true for low-dimensional semiconductors, where excitons are the primary charge carriers and  $E_b$  is correlated with many other important properties, such as exciton and charge-carrier lifetimes, absorption strength, PL quantum yield, etc. The last decade has seen significant research interest in monolayer transition metal dichalcogenides (TMDC) and 2D halide perovskites (HPs), largely because of the unique and tunable properties of the 2D Wannier excitons that are hosted in these systems. <sup>1–3</sup> However, the large variance in reported  $E_b$  for the same material (e.g., 180–490 meV<sup>4–9</sup> for BA<sub>2</sub>PbI<sub>4</sub> [where BA = butylammonium]) forces one to conclude that either  $E_b$  is highly dependent on extrinsic conditions or  $E_b$  measurement methods are less trustworthy, as is often assumed.

In a complementary review article, we highlight the challenges associated with various  $E_b$  measurement techniques in an attempt to reconcile the large variance in reported  $E_b$  for monolayer TMDCs and 2D HPs<sup>10</sup> and show that the variance in

#### **PROGRESS AND POTENTIAL**

The properties of excitons underpin the absorption, emission, and energy transfer properties of quantum well systems. For GaAs-based quantum wells in the 1980s and 1990s, mapping the relationships between the exciton properties and the quantum well structure allowed control of these optoelectronic properties and ultimately led to invention of bluelight-emitting diodes and the 2014 Nobel Prize in Physics. For quantum well systems of today, such as 2D perovskites, there is a large variance in the reported values of the exciton's properties, both measured and calculated. Here, we solve this issue by obtaining unambiguous measurements of the exciton properties. By repeating these measurements on a large number of structures, we map the relationships between exciton properties and the underlying quantum well structure. This allows us to determine the correct theory for calculating exciton properties and ultimately enables control of these properties.







reported  $E_b$  is mostly due to inaccurate measurements. In this research article, we use electroabsorption (EA) to directly measure  $E_b$  and  $E_g$  of 2D HPs in a manner than is precise and supported unambiguously by established Elliott theory and Franz-Keldysh theory. The tunable nature of HPs allows us to repeat these measurements while varying essentially every parameter that has been proposed to affect  $E_b$  in 2D semiconductors and quantify their effects on  $E_b$ , such as barrier polarizability, well polarizability, barrier length, well length, morphology, temperature, octahedral tilting, etc. The large sample size of 31 materials combined with the high quality of measurement allows us to critically test theories of excitons in low-dimensional systems, test theories of excitons in ionic lattices, and explore correlations between  $E_a$  and  $E_b$ .

#### **RESULTS AND DISCUSSION**

We studied the electric field dependence of band-edge absorption features for a variety of HP compositions. Polycrystalline thin films were spin coated onto an array of electrodes, and the absorption and EA (the difference in absorption between electric field on vs. off) spectra were collected at 15 K using external electric fields parallel to the HP layers (see Experimental procedures). The absorption spectrum of the archetypical 2D HP compound BA<sub>2</sub>PbI<sub>4</sub> is shown in Figure 1A, where a step-like feature is resolved near 2.8 eV with an electric field dependence (Figure 1B), similar to the continuum edge of a theoretical 2D Wannier exciton in an electric field (Figure 1C). The latter was calculated by solving the Schrödinger equation for a 2D electron-hole pair in a uniform electric field and relating the wavefunction solutions to the semiconductor's absorption through Elliott's formula 11,12 (Note S1). Therefore, the simulation can be viewed as a generalized expectation for the electric field response of a 2D semiconductor's interband transition when absorption broadening is low and the electric field perturbation is small compared with the exciton's ionization energy it contains no material-specific assumptions or fit parameters. The feature's physical origin is the Franz-Keldysh (FK) effect, which is rendered clearly from the simulation and the field dependence of the feature, as shown in Figure 1D for 65–150 kV/cm. In comparison with the exciton features (labeled  $x_1$  and  $x_2$ ), which originate from the Stark effect, the points within the FK feature (labeled a-e) have amplitudes with weaker field dependence (Figure 1E) and separations with greater field dependence (Figure 1F), both of which are predicted by theory and are consequences of applying an electric field to unbound electronic states; i.e., the FK effect. 13-16 The electric field transforms the conduction and valence band Bloch functions into Airy functions, resulting in a transfer of oscillator strength from above the gap (point c) to below the gap (point a). The crossover point is an exact measurement of the one-electron band-gap energy ( $E_a$ ). In the dimensionless units of the simulation, this occurs at  $(E - E_g)/R = 0$ ; accordingly, we assign  $E_g$  to the zero-crossing point b in Figure 1B, which is 2.828  $\pm$  0.002 eV. The exciton  $E_b$  is then readily determined by  $E_b = E_g E_{1s}$ , where  $E_{1s}$  is the resonance energy of the 1s exciton taken from the exciton absorption peak. The resulting  $E_{\rm b}$  measurement of 256  $\pm$  4 meV is precise and unambiguous and is about half the value of most reports in the literature.<sup>4-7</sup>

Before studying the variation in  $E_b$  between different materials, we first investigate whether this measurement method is affected by the polycrystalline nature of the thin films (which is necessitated by our EA geometry) by comparing the  $BA_2PbI_4$  thin film absorption with that of a single crystal. The thin film absorption in Figure 1G (black) has a step-like feature that is matched in the photoluminescence excitation (PLE) spectrum of a single crystal (SC) flake measured by Blancon et al. (blue). The FK oscillation in the thin-film EA at the same energy confirms that the step

<sup>&</sup>lt;sup>1</sup>Department of Chemistry, University of Utah, Salt Lake City, UT 84112, USA

<sup>&</sup>lt;sup>2</sup>Department of Materials Science and Engineering and Materials Research Laboratory, University of Illinois at Urbana-Champaign, Urbana, IL 61801, USA

<sup>&</sup>lt;sup>3</sup>Department of Physics and Astronomy, Brigham Young University, Provo, UT 84602, USA

<sup>&</sup>lt;sup>4</sup>National Renewable Energy Laboratory, Golden, CO 80401, USA

 $<sup>^5</sup>$ Los Alamos National Laboratory, Los Alamos, NM, USA

<sup>&</sup>lt;sup>6</sup>These authors contributed equally

<sup>&</sup>lt;sup>7</sup>Lead contact

<sup>\*</sup>Correspondence: kameron.hansen@utah.edu https://doi.org/10.1016/j.matt.2023.07.004



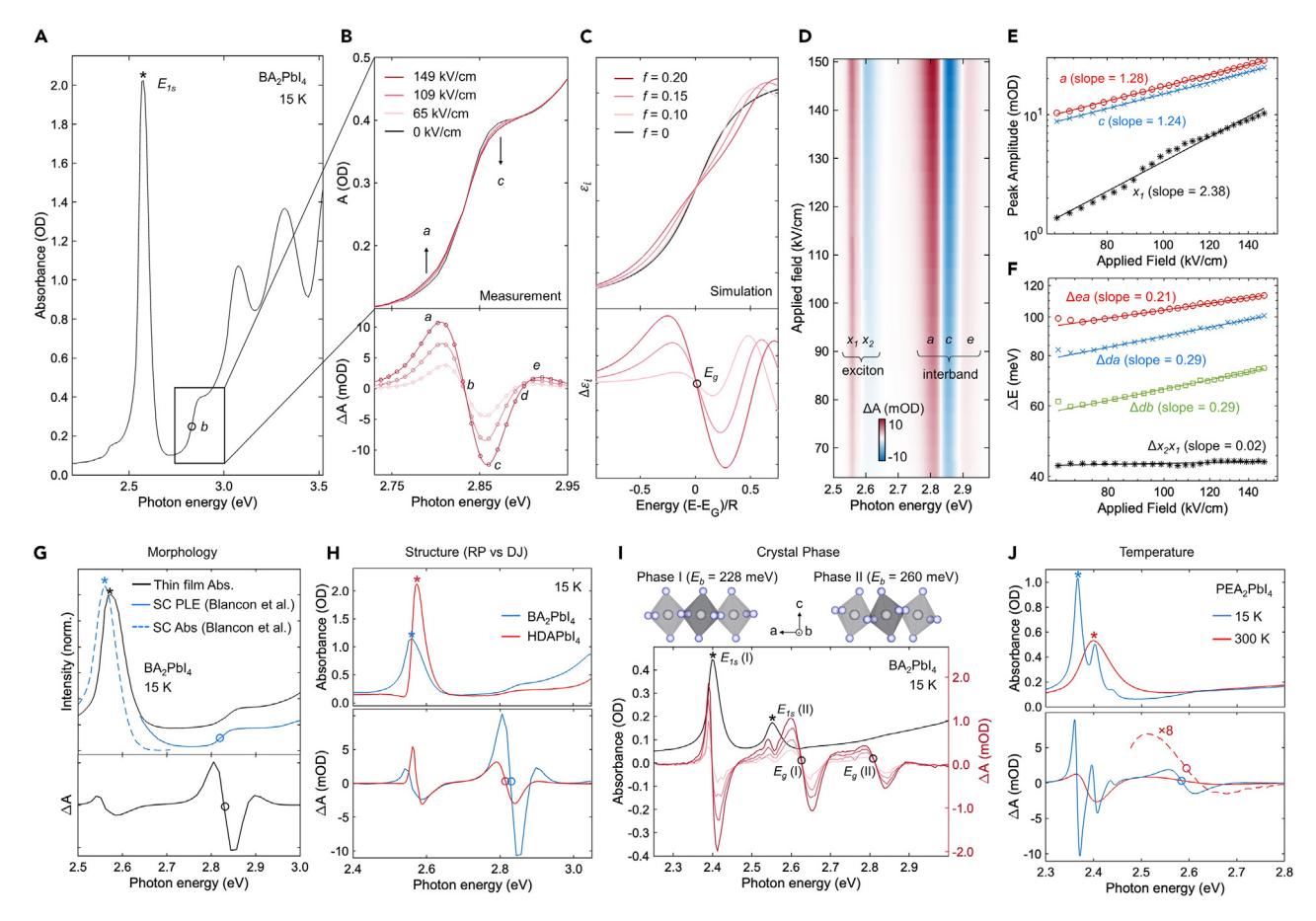


Figure 1. Precise  $E_q$  and  $E_b$  measurements enabled by the FK effect

- (A) Absorption of a BA<sub>2</sub>PbI<sub>4</sub> thin film at 15 K.
- (B) A magnification of the electric field dependence of the step-like absorption feature at the interband transition (top) and corresponding EA signal (difference between field on vs. off; bottom).
- (C) The field dependence of a theoretical 2D Wannier exciton's interband absorption (top) and the corresponding EA signal (bottom).
- (D) The field dependence of the EA spectrum from  $65-150~\mathrm{kV/cm}$ .
- (E) The amplitudes of the interband (a and c) and exciton  $(x_1)$  EA peaks as a function of applied field.
- (F) The spectral separation of interband ( $\Delta ea$ ,  $\Delta da$ , and  $\Delta db$ ) and exciton ( $\Delta x_2 x_1$ ) EA features as a function of applied field.
- (G) Absorption of our BA<sub>2</sub>Pbl<sub>4</sub> thin film compared with the absorption and PLE spectra of an SC flake reported in Blancon et al. (top) and the thin film EA (bottom). Our assignments of  $E_{1s}$  and  $E_{g}$  are marked by open circles and asterisks, respectively. See also Figures S1, S2, and S3.
- (H) Comparison of the  $BA_2PbI_4$  absorption and EA with those of HDAPbI\_4, a DJ 2D HP.
- (I) Absorption and EA of a BA<sub>2</sub>PbI<sub>4</sub> thin film that retained a large portion of crystallites in the room-temperature phase (phase I) after cooling to 15 K. The octahedral tilting in phase II increases  $E_b$  by 32 meV. See also Figure S4.
- (J) Absorption and EA of a PEA<sub>2</sub>PbI<sub>4</sub> thin film at 15 K and 300 K, showing that temperature has only a small effect on  $E_b$ . The dashed line is an 8 × amplification of the 300-K spectrum. See also Figures S5 and S6.

feature's origin lies in an interband transition. As demonstrated in Figure S1, the midpoint of the step is a trustworthy marker of  $E_g$ . Thus,  $E_b$  can be estimated in the SC flake by the spectral separation between  $E_g$  (open circle) and  $E_{1s}$  (asterisk), resulting in  $E_b = 259 \pm 15$  meV, which agrees with our thin-film measurement of  $256 \pm 4$  meV. In Note S3, we present our own SC measurements as well as EA measurements on five thin films with varying degrees of morphological disorder. The results further demonstrate that  $E_b$  is independent of sample morphology and disconfirm the hypothesis that  $E_b$  is affected by microstructure in HPs.  $^{17,18}$ 

Replicating this measurement technique for other HP structures is made easy by the fact that the FK feature is universally observed in the EA response of all 2D HPs. For





	Organic cation	d <sub>002</sub> (Å)	$\epsilon_{\infty}$	$\boldsymbol{\varepsilon}_0$	$arepsilon_{MHz}$	$\mu$ (m <sub>0</sub> )	$E_g$ (eV)	$E_b$ (meV)	$\langle r \rangle$ (Å)
BA <sub>2</sub> PbI <sub>4</sub> (I)	butylammonium	13.81	3.19	7.06		0.111	$2.626 \pm 0.004$	228 ± 5	13.9
BA <sub>2</sub> PbI <sub>4</sub> (II)	butylammonium	13.04	3.30	6.70	11.2	0.139	$2.831 \pm 0.002$	$256\pm4$	13.2
(C <sub>5</sub> ) <sub>2</sub> PbI <sub>4</sub> (II)	amylammonium	14.52					$2.845 \pm 0.002$	$272 \pm 5$	12.8
(C <sub>6</sub> ) <sub>2</sub> PbI <sub>4</sub> (I)	hexylammonium	16.35					$2.579 \pm 0.004^{a}$	$235 \pm 6^{a}$	13.7
(C <sub>7</sub> ) <sub>2</sub> PbI <sub>4</sub> (I)	heptylammonium	18.31			10.1		$2.627 \pm 0.008$	246 ± 9	13.4
(C <sub>7</sub> ) <sub>2</sub> PbI <sub>4</sub> (II)	heptylammonium	17.12	2.99	6.69		0.147	$2.844 \pm 0.002$	$277\pm4$	12.7
(C <sub>10</sub> ) <sub>2</sub> PbI <sub>4</sub> (II)	decylammonium	21.21	2.77	5.11	8.2	0.141	$2.878 \pm 0.003$	$298\pm4$	12.3
(C <sub>12</sub> ) <sub>2</sub> PbI <sub>4</sub> (II)	dodecylammonium	24.51					$2.869 \pm 0.002$	$292 \pm 3$	12.4
(C <sub>14</sub> ) <sub>2</sub> PbI <sub>4</sub> (II)	tetradecylammonium	27.08	2.42			0.135	$2.882 \pm 0.003$	$297 \pm 4$	12.3
(C <sub>16</sub> ) <sub>2</sub> PbI <sub>4</sub> (II)	hexadecylammonium	29.65					$2.877 \pm 0.003$	$300 \pm 4$	12.2
PEA <sub>2</sub> PbI <sub>4</sub>	phenethylammonium	16.34	3.29	6.18	10.5	0.108*	$2.589 \pm 0.004$	$223 \pm 4$	14.1
EOA <sub>2</sub> PbI <sub>4</sub>	ethanolammonium	10.05	3.94	13.61		0.122	$2.378 \pm 0.005$	55 ± 7	30.1
TEA <sub>2</sub> PbI <sub>4</sub>	thiopheneethylammonium	15.75					$2.607 \pm 0.004$	$218 \pm 4$	14.2
5F-PEPI	5-fluoro-phenethylammonium	16.82	3.03				$2.759 \pm 0.002$	$274\pm3$	12.7
HDAPЫ₄	hexamethylenediammonium	25.96					$2.817 \pm 0.003$	$248 \pm 5$	13.4
BA <sub>2</sub> SnI <sub>4</sub>	butylammonium	13.06	3.47	10.04		0.097	$2.35 \pm 0.02$	$170 \pm 20$	16.2
PEA <sub>2</sub> SnI <sub>4</sub>	phenethylammonium	16.35					$2.11 \pm 0.015$	$138 \pm 15$	19.1
PEA <sub>2</sub> SnBr <sub>4</sub>	phenethylammonium	16.61					$3.151 \pm 0.006$	$276 \pm 6$	12.7
BA <sub>2</sub> PbBr <sub>4</sub>	butylammonium	13.81	2.61	6.31		0.132	$3.392 \pm 0.002$	$352 \pm 4$	11.4
PEA <sub>2</sub> PbBr <sub>4</sub>	phenethylammonium	16.67	2.74	5.86	6.1	0.1	$3.425 \pm 0.003$	$349 \pm 4$	11.4
PEA <sub>2</sub> PbBr <sub>3.3</sub> Cl <sub>0.6</sub>	phenethylammonium	16.75					$3.512 \pm 0.006$	$380 \pm 8$	10.9
PEA <sub>2</sub> PbBr <sub>2.6</sub> Cl <sub>1.3</sub>	phenethylammonium	16.90					$3.639 \pm 0.008$	$405 \pm 9$	10.6
PEA <sub>2</sub> PbBr <sub>2</sub> Cl <sub>2</sub>	phenethylammonium	16.65					$3.837 \pm 0.006$	$439 \pm 8$	10.0
PEA <sub>2</sub> PbBr <sub>1</sub> Cl <sub>3</sub>	phenethylammonium	16.74					$4.005 \pm 0.005$	$465 \pm 6$	9.9
PEA <sub>2</sub> PbCl <sub>4</sub>	phenethylammonium	16.89	2.48	5.62	6.9	0.118	$4.13 \pm 0.008$	$487 \pm 9$	9.6
BA <sub>2</sub> PbCl <sub>4</sub>	butylammonium	13.99	2.27	5.90					
BA <sub>2</sub> MAPb <sub>2</sub> I <sub>7</sub>	butylammonium	19.67	3.33	9.84			$2.325 \pm 0.015$	135 $\pm$ 16	18.5
(C <sub>6</sub> ) <sub>2</sub> MAPb <sub>2</sub> I <sub>7</sub>	hexylammonium						$2.272 \pm 0.015$	114 $\pm$ 16	19.3
BA <sub>2</sub> MA <sub>2</sub> Pb <sub>3</sub> I <sub>10</sub>	butylammonium	25.98	3.97				$2.12 \pm 0.02^{a}$	$77 \pm 25^{a}$	25.6
(C <sub>6</sub> ) <sub>2</sub> MA <sub>2</sub> Pb <sub>3</sub> I <sub>10</sub>	hexylammonium						$2.120 \pm 0.015^{a}$	$97 \pm 17^{a}$	22.3
MAPbl <sub>3</sub>	methylammonium		4.53 <sup>b</sup>		37	0.104 <sup>c</sup>	1.636 <sup>c</sup>	16 ± 2°	43.0
MAPbBr <sub>3</sub>	methylammonium		3.55 <sup>b</sup>		26 <sup>d</sup>	0.13 <sup>e</sup>	$2.317 \pm 0.006$	$28 \pm 6$	38.2
MAPbCl <sub>3</sub>	methylammonium		2.87 <sup>b</sup>		24 <sup>d</sup>	0.18 <sup>e</sup>	$3.088 \pm 0.008$	67 ± 9	27.5

<sup>&</sup>lt;sup>a</sup>Based on our analysis of EA spectra reported in Tanaka and Kondo. <sup>40</sup>

example, as shown in Figure 1H, the EA response of the Dion-Jacobson (DJ) structure HDAPbI<sub>4</sub> (HDA = hexamethylenediammonium; abbreviations for subsequent cations are listed in Table 1) is qualitatively identical to that of its Ruddlesden-Popper (RP) counterpart BA<sub>2</sub>PbI<sub>4</sub>, with two primary oscillations: a Stark shift of the exciton below  $E_g$  and the FK feature at  $E_g$ . The spectral separations between the Stark and FK features (i.e.,  $E_b$ ) are very similar, which is somewhat coincidental because  $E_b$  is sensitive to a wide range of factors. For example, even for the same BA<sub>2</sub>PbI<sub>4</sub> composition,  $E_b$  changes by 32 meV when moving across its phase transition near ~230 K<sup>19</sup> (Figure 1I). This BA<sub>2</sub>PbI<sub>4</sub> film contained some crystallites in the room-temperature (I) phase and others in the low-temperature phase (II) upon cooling to 15 K. Because both crystal phases produced their own FK feature (labeled  $E_g$ (I) and  $E_g$ (II) in Figure 1I), this allowed simultaneous  $E_b$  measurements of phase I and II structures with all other variables held constant. The 32 meV increase in  $E_b$  moving from phase I  $\rightarrow$  II can be understood in terms of the increase in the octahedral tilt angle (depicted at the top of Figure 1I). As detailed in Note S4, we discovered

<sup>&</sup>lt;sup>b</sup>Leguy et al.<sup>33</sup>

<sup>&</sup>lt;sup>c</sup>Miyata et al.<sup>41</sup>

<sup>&</sup>lt;sup>d</sup>Poglitsch and Weber.<sup>64</sup>

eBokdam et al.65



that the degree of octahedral tilt is strongly correlated with the exciton's reduced effective mass ( $\mu$ ) for all 2D HPs, and in this case, the 23° increase in the octahedral tilt angle moving from phase I  $\rightarrow$  II is associated with a 25% increase in  $\mu$ . Because  $E_b \propto \mu$ , this causes  $E_b$  to also increase. Similar measurements were obtained for a related 2D HP composition that further confirmed the effect of the octahedral tilt on  $E_b$  (Figure S4).

The effect of temperature on  $E_b$  without structural phase transitions as a confounding variable can be determined by turning to PEA<sub>2</sub>PbI<sub>4</sub>, another archetypical 2D HP compound that, unlike its BA counterpart, does not undergo any phase transitions between 300 K and 15 K. As shown in Figure 1J, the PEA<sub>2</sub>PbI<sub>4</sub> absorption and EA features redshift upon cooling, but  $E_b$  remains fairly constant by comparison. By simulating the effect of temperature on the EA signal (Figure S5) and repeating this measurement for several samples (Figure S6), we conclude that  $E_b$  increases by 9%  $\pm$  3% upon cooling from 300 K to 15 K, which implies that the polarization mechanisms responsible for screening the electron-hole interactions in HPs have only a weak temperature dependence. Because the origin of the EA features are unambiguous and have widths determined purely by lifetime broadening, <sup>20</sup> these are among the clearest indicators of morphological and temperature effects on  $E_b$  in any material system to date.

Having established that  $E_b$  is largely unaffected by extrinsic conditions, we seek to map the relationships between  $E_b$  and the intrinsic material parameters that do dictate its value. Because 2D HPs are quantum well systems that consist of alternating organic (barrier) and inorganic (well) layers, these parameters include the exciton's reduced mass ( $\mu$ ), the dielectric constant of the well and barrier ( $\varepsilon_w$ ,  $\varepsilon_b$ ), the length of the well  $(l_w)$ , and possibly the length of the barrier  $(l_b)$ .<sup>21</sup> In Figure 2A, the absorption and EA of lead-iodide 2D HPs with different barrier molecules are presented with  $E_{1s}$  and  $E_{q}$  assignments, marked by asterisks and open circles, respectively. Previous studies have used molecules such as ethanolamine (EOA; purportedly high  $\varepsilon_b$ ), <sup>6,22</sup> 2-thiopheneethylamine (TEA; purportedly low  $\varepsilon_b$ ), <sup>23</sup> and fluorinated phenylethylamine (PEA; purportedly low  $\varepsilon_b$ )<sup>24</sup> to tune the dielectric mismatch; however, this strategy for controlling  $E_b$  is poorly understood because of uncertainty surrounding the correct values of  $\varepsilon_w$  and  $\varepsilon_b$  as well as the functional relationship between  $E_b$  and the dielectric mismatch ( $\varepsilon_w/\varepsilon_b$ ). The confounding variable of  $I_b$  is typically ignored,  $^{21}$  but the data in Figure 2A show  $E_b$  trending upward with molecule length and suggest that a relationship may exist between  $E_b$  and  $I_b$ . While precisely mapping these relationships is a goal of this study and is addressed later, for now we simply observe that the variation in  $E_b$  is moderate, and  $E_b$  appears to increase as  $I_b$ increases. Moving to the inorganic layer, we see that chemical substitutions in this layer have an even larger effect on  $E_b$  and  $E_g$ . In the bottom panel of Figure 2A, the EA and absorption results are presented for PEA2BX4 structures where the organic cation PEA is held constant while the composition of the well layer is changed. The blueshifting of the band gap moving from  $[Snl_4]^{2-} \rightarrow [Pbl_4]^{2-} \rightarrow$  $[PbBr_4]^{2-} \rightarrow [PbCl_4]^{2-}$  is clearly matched with a concomitant increase in  $E_b$ . The well length for each of these structures is quite consistent ( $I_w = 6.40 \pm 0.01 \text{ Å}$ ); thus, these significant changes to  $E_g$  and  $E_b$  are driven by changes in  $\varepsilon_w$ .

Using EA in this fashion, we obtained highly accurate  $E_g$  and  $E_b$  values for 31 unique HP compounds. The numerical values are given in Table 1, and 18 of the 2D HPs are plotted in Figure 2B; the others are discussed in conjunction with Figure 4 below. These  $E_b$  measurements are among the most precise (lowest relative uncertainty) for any material system to date; therefore, they provide the opportunity to critically



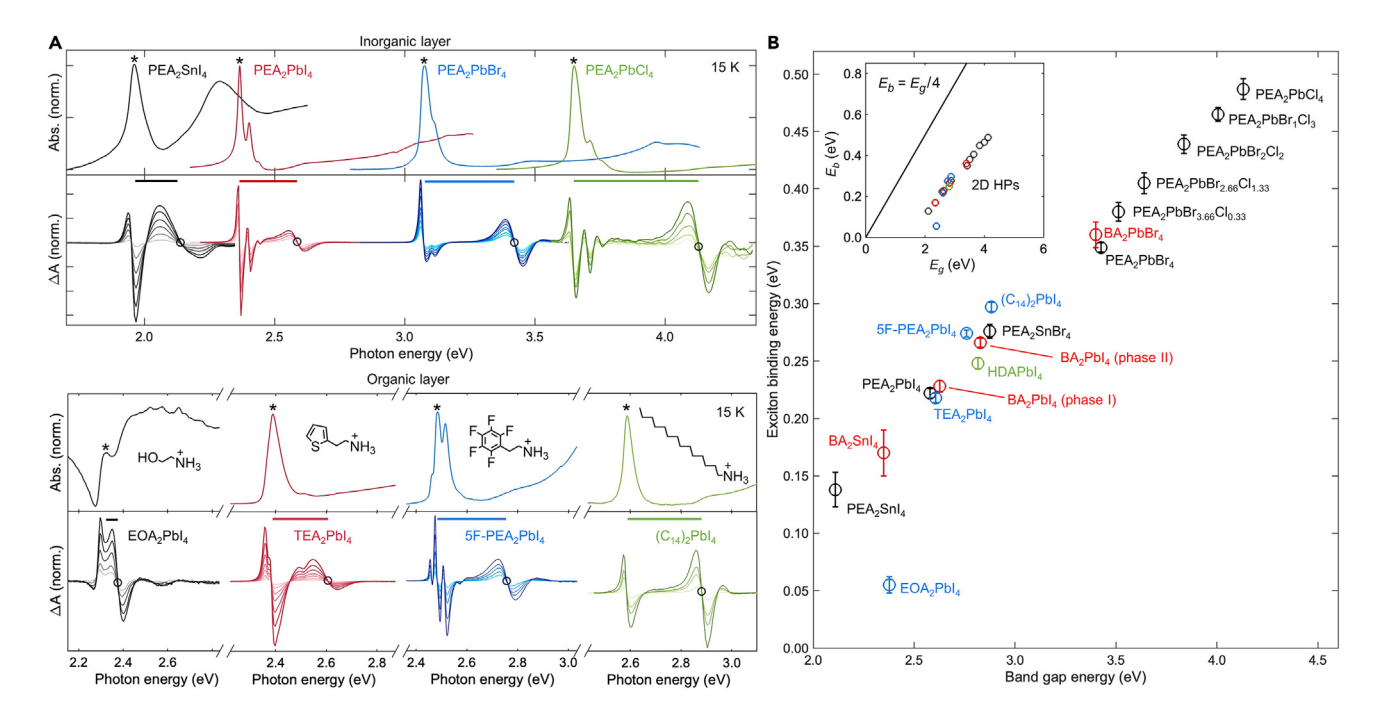


Figure 2.  $E_g$ - $E_b$  correlation

(A) Top: absorption and EA of lead iodide 2D HPs with various organic cations. The solid horizontal bars span from  $E_{1s}$  to  $E_g$  and represent the magnitude of  $E_b$ . Bottom: absorption and EA of PEA<sub>2</sub>SnI<sub>4</sub>, PEA<sub>2</sub>PbI<sub>4</sub>, PEA<sub>2</sub>PbBI<sub>4</sub>, and PEA<sub>2</sub>PbCI<sub>4</sub>.

(B)  $E_b$  as a function of  $E_g$  for 18 unique 2D HP compositions, obtained from absorption and EA at 15 K. Error bars denote one standard deviation. The top inset shows the 2D HP trend in comparison to the universal scaling of  $E_g = 0.25E_b$  for 2D semiconductors.

test solid-state theories and map the relationships between E<sub>b</sub> and the material parameters. While these tasks are taken on in the remainder of the article, we first point out a striking correlation: a linear trend emerges when  $E_b$  is plotted as a function of  $E_g$  (Figure 2B). A similar scaling between  $E_g$  and  $E_b$  was recently predicted in a theoretical study by Jiang et al., <sup>25</sup> where the authors used k·p theory to derive a trendline of  $E_b = 0.25E_q$  for inorganic 2D semiconductors suspended in a vacuum. Their derived trendline is supported by first-principles Bethe-Salpeter equation (BSE) calculations. While the results in Figure 2B validate the concept of an  $E_q$ - $E_b$ correlation in 2D semiconductors and extend it to HPs, the measured trend of  $E_b$  = 0.180 $E_g$  - 0.249 deviates from Jiang et al.'s<sup>25</sup> theoretically predicted trend of  $E_b$  = 0.25 $E_g$  by its lower slope and its non-zero, negative y intercept. However, the reasons for these deviations are not clear. Not only is the evolution of the fundamental material parameters ( $\varepsilon_{w}$ ,  $\varepsilon_{b}$ ,  $l_{w}$ ,  $l_{b}$ , and  $\mu$ ) between the different 2D HPs unknown, but additionally, the manner in which these parameters affect  $E_g$  and  $E_b$  is an open question, especially considering that the results in Figure 2A suggest a relationship between  $E_b$  and  $I_b$ , which contradicts leading theoretical models for excitons in 2D HPs.<sup>21</sup> Therefore, we aim to determine the material parameters, calculate  $E_b$  and  $E_a$  for each structure, and test whether the experimental results can be reproduced by theory to gain a deeper understanding.

To determine  $I_w$  and  $I_b$ , X-ray diffraction (XRD) patterns were collected for each 2D HP structure, and the interlayer (d<sub>002</sub>) spacing was verified to be in agreement with single-crystal XRD in the literature (Figure S25). The nominal well length ( $I_w$ ) is taken as the distance between opposing halide atoms in a [BX<sub>4</sub>]<sup>2-</sup> layer and the barrier length as  $I_b = d_{002} - I_w$ .  $\mu$  was determined from the curvature of the band minima computed via density functional theory (DFT) (Note S10). The dielectric constant



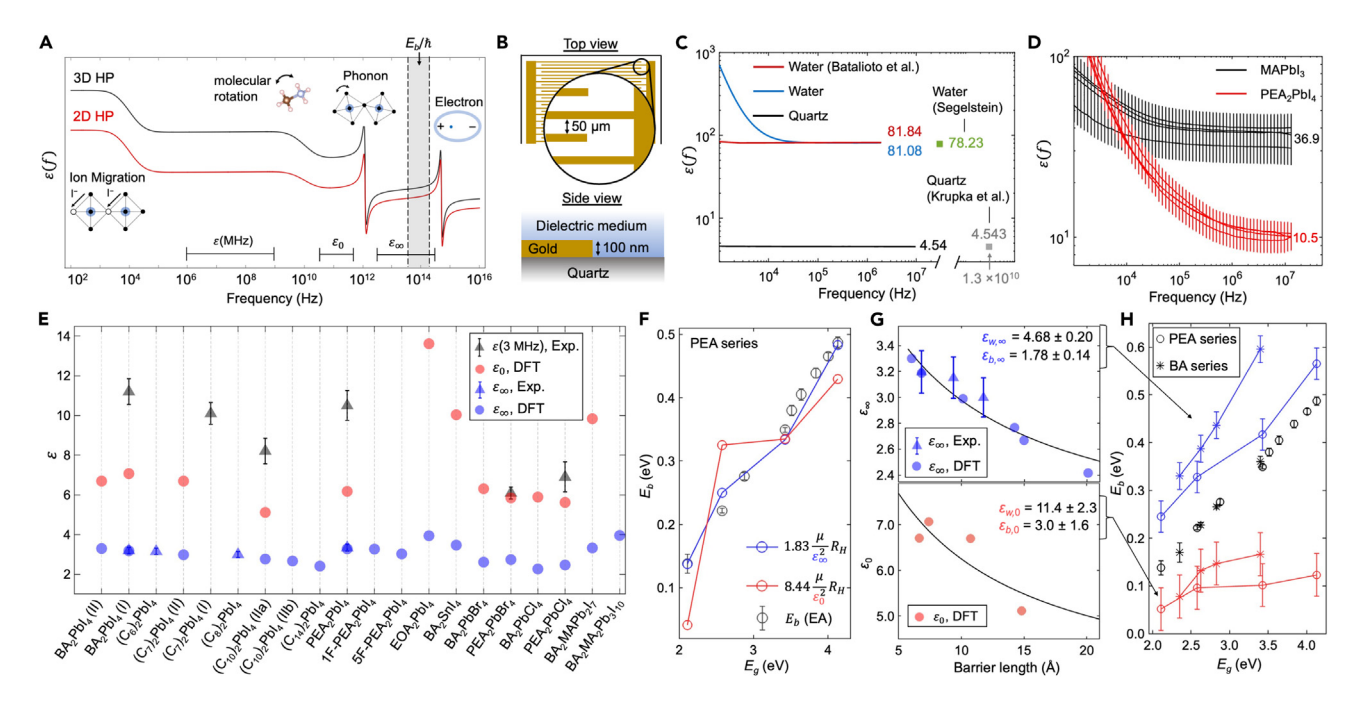


Figure 3. Dielectric properties of 2D HPs

- (A) A representation of the real part of the dielectric function  $\varepsilon(f)$  for 2D and 3D HPs, informed by multiple literature reports (Supplemental section 8).
- (B) A schematic of our IDE substrates used to measure the dielectric constant.
- (C) IDE measurements of water and quartz compared with those in Batalioto et al., <sup>61</sup> Segelstein, <sup>62</sup> and Krupka et al. <sup>63</sup>
- (D) IDE measurements of MAPbl<sub>3</sub> (4 samples) and PEA<sub>2</sub>Pbl<sub>4</sub> (4 samples)Error bars denote one standard deviation.
- (E) Comparison of  $\epsilon$ (3 MHz) obtained by IDE measurements (black triangle),  $\epsilon_0$  obtained by DFT (red circles),  $\epsilon_\infty$  obtained by mR measurements in DeCrescent et al. 29 (blue triangles), and  $\epsilon_\infty$  obtained from DFT (blue circles). Error bars denote one standard deviation.
- (F)  $E_b$  as a function of  $E_q$  for PEA-based 2D HPs alongside a fitted Wannier model using  $\varepsilon_0$  (red) and  $\varepsilon_\infty$  (blue) values.
- (G) The dielectric constants for multiple members of the  $(C_m)_2$ PbI $_4$  series as a function of barrier length, with fit (solid line) used to obtain  $\varepsilon_w$  and  $\varepsilon_b$ . Error bars denote one standard deviation.
- (H) Experimental  $E_b$  values as a function of  $E_g$  for the PEA- and BA-series plotted in comparison to theoretical  $E_b$  values calculated using  $\varepsilon_{w,\infty}$  and  $\varepsilon_{b,\infty}$  (blue) and  $\varepsilon_{w,0}$  and  $\varepsilon_{b,0}$  (red). Error bars denote one standard deviation.

and  $\mu$  are the most consequential factors that dictate  $E_b$ ; i.e., in the Wannier model:  $E_b = (\mu/\epsilon^2)R_H$ , where  $R_H$  is the hydrogen Rydberg energy (~13.6 eV). However,  $\epsilon$  is itself a function of frequency (Figure 3A). A long-standing question has been the value of the dielectric function that determines  $E_b$ . Standard solid-state theories assume that the frequency of interest corresponds to the  $E_b f \sim E_b/\hbar$  (Figure 3A, shaded region) under the rationale that polarization mechanisms with characteristic frequencies below  $E_b/\hbar$  are too slow to screen the electron-hole relative motion. <sup>26,27</sup> However, this assumption has largely evaded experimental verification because of the difficulty of simultaneously obtaining high-confidence measurements of  $E_b$ ,  $\varepsilon$ , and  $\mu$  in systems where  $\varepsilon_0$  and  $\varepsilon_\infty$  differ meaningfully, where  $\varepsilon_0$  and  $\varepsilon_\infty$  refer to the dielectric constant below and above the phonon resonance ( $\omega_{LO}$ ), respectively. Unlike covalently bonded III-V semiconductors, where  $\varepsilon_0$  and  $\varepsilon_\infty$  are nearly identical, the ionic lattice of 2D HPs is very polarizable, leading to a doubling of the dielectric constant across the phonon resonance ( $\varepsilon_0 \sim 2\varepsilon_\infty$ ). Thus, in this regard, 2D HPs are an ideal system to test this question, and the accurate  $E_b$  measurements here place us in a unique position to do so, provided that the dielectric constants can be determined across a wide frequency range.

For the low-frequency (MHz) range, we developed a new method for performing dielectric spectroscopy on thin films based on an interdigitated electrode (IDE) geometry (Figure 3B). Our IDE approach, explained in Note S9, produced





 $\varepsilon$ (3 MHz) = 81.08 for water and 4.54 for quartz, which agree closely with literature values (Figure 3C). Applying the IDE method to MAPbI<sub>3</sub> and PEA<sub>2</sub>PbI<sub>4</sub> results in  $\varepsilon$ (3 MHz) values of 36.9  $\pm$  7.0 and 10.5  $\pm$  1.5 respectively (Figure 3D). Repeating these measurements for other compounds, we found  $\varepsilon$ (3 MHz) to be consistently larger than  $\varepsilon$ <sub>0</sub> (Figure 3E), where the latter refers to the dielectric constant below  $\omega_{LO}$ , which we calculated via DFT using the semi-local generalized-gradient approximation to describe exchange and correlation. This discrepancy indicates that the azimuthal rotation of the barrier molecules contributes to the dielectric response in 2D HPs similar to the rotation of methylammonium (MA) in 3D HPs, and this interpretation is supported by MD simulations.<sup>28</sup> The high-frequency dielectric constants ( $\varepsilon_{\infty}$ ) were also obtained from DFT, and these values (Figure 3E, blue circles) agree very closely with recent measurements by DeCrescent et al.,<sup>29</sup> where a Kramers-Kronig-consistent combination of momentum-resolved reflectance (mR) and ellipsometry was used to obtain precise values at 2 × 10<sup>14</sup> Hz (Figure 3E, blue triangles).

We apply these dielectric constants to a modified Wannier equation,  $E_b = \gamma (\mu/\epsilon^2) R_H$ , to gain insight into the large increase in  $E_b$  moving from  $PEA_2SnI_4 \rightarrow PEA_2PbI_4 \rightarrow$ PEA<sub>2</sub>PbBr<sub>4</sub> $\rightarrow$ PEA<sub>2</sub>PbCl<sub>4</sub>. Here,  $\gamma$  is a fit parameter;  $\mu$  and  $E_b$  are known from DFT and experiments, respectively; and  $\varepsilon_{\infty}$  and  $\varepsilon_{0}$  are tested to see which best captures the upward trend in  $E_b$  (Figure 3F). While  $\varepsilon_{\infty}$  and  $\varepsilon_0$  result in reasonable fits, the fit is better for  $\varepsilon_{\infty}$ , which suggests that  $\varepsilon_{\infty}$  is responsible for the majority of the exciton screening, and this result is reproduced for the BA series of compounds (Figure S28). More interesting than the goodness of fit, however, is the fitted value itself ( $\gamma$  = 1.83 using  $\varepsilon_{\infty}$  and  $\gamma$  = 8.44 using  $\varepsilon_{0}$ )because this factor represents the degree to which excitons in 2D HPs deviate from the Wannier model. Indeed, significant deviations are expected because of independent quantum and dielectric confinement effects that greatly enhance  $E_b$  in 2D HPs.<sup>21</sup> In a true 2D system, quantum confinement increases  $E_b$  by 4 and dielectric confinement by  $(\varepsilon_w/\varepsilon_b)2.^{30}$  Using standard values for lead-iodide compounds ( $\varepsilon_w \sim 5$  and  $\varepsilon_b \sim 2$ ) leads to  $\gamma = 4(5/2)^2 = 25$ , which is undoubtably an overestimation considering the non-zero width (6.4 Å) of the inorganic layers. To solve for  $\gamma$  in a more realistic quasi-2D case and, hence, make possible calculations of  $E_b$ for arbitrary wells and barriers, we seek to model the excitons in 2D HPs.

Modeling dielectric confinement requires knowledge of the barrier and well dielectric constants distinct from those of the bulk. 31 Previous studies on 2D HPs have estimated  $\varepsilon_w$  and  $\varepsilon_b$  from DFT-based calculations of the dielectric profile or dielectric constants of the analogous subsystems (e.g., bulk PbI<sub>2</sub> as a surrogate for  $[PbI_4]^{2-}$ ). And we take a new approach, shown in Figure 3G, where values of  $\varepsilon_w$  for  $[Pbl_4]^{2-}$  and  $\varepsilon_b$  for  $[(C_m)_2]^{2-}$  are obtained by fitting a series of  $(C_m)_2Pbl_4$ structures to the spatially averaged dielectric constant of a layered material:  $\varepsilon_{bulk} = (\varepsilon_w l_w + \varepsilon_b l_b)/(l_w + l_b)$ . Here,  $C_m$  denotes alkylammonium chains of varying lengths ( $C_m = CH_3[CH_2]_{m-1}NH_3$ ), where m = 4 is the previously discussed BA molecule. The lengths  $l_w = 6.4$  Å and 6.7 Å  $< l_b < 23.3$  Å are known from XRD, and for eight materials,  $\varepsilon_{bulk}$  is known from DFT and/or experiments. The fitting uncertainties for  $\varepsilon_w$  and  $\varepsilon_b$  (shown in Figure 3G) are relatively small, which indicates that solving for  $\varepsilon_{\rm w}$  and  $\varepsilon_{\rm b}$  according to the spatially averaged equation can be done in a self-consistent manner. With knowledge of  $\varepsilon_w$  for  $[Pbl_4]^{2-}$  and  $\varepsilon_b$  for  $[(C_m)_2]^{2+}$  at frequencies above and below  $\omega_{LO}$ , the dielectric constants of the other inorganic layers  $([SnI_4]^{2-}, [PbBr_4]^{2-}, [PbCl_4]^{2-})$  and organic layers  $([EOA_2]^{2+}, [PEA_2]^{2+}, [5F-PEA_2]^{2+})$ can be solved for in a similar manner at both frequencies (Note S11). The  $\varepsilon_{w,\infty}$  values obtained for  $[Pbl_4]^{2-}$ ,  $[PbBr_4]^{2-}$ , and  $[PbCl_4]^{2-}$  layers (4.68, 3.45, and 2.79, respectively) are very close to  $\varepsilon_{\infty}$  determined by ellipsometry for MAPbI<sub>3</sub>, MAPbBr<sub>3</sub>, and MAPbCl<sub>3</sub> (4.53, 3.55, and 2.87, respectively),<sup>33</sup> which is expected because the



electronic structure of the  $[PbX_4]^{2-}$  layers and MAPbX<sub>3</sub> structures originates from the same  $[BX_6]^{4-}$  octahedral unit, and this agreement serves as a helpful validation of our methodology.

To model the exciton properties,  $\varepsilon_w$  and  $\varepsilon_b$  are used to construct a potential for the electron-hole interaction within a superlattice of dielectric and quantum wells, and E<sub>b</sub> is obtained by solving the resulting quasi-2D Schrödinger equation (Note S12). This is a more generalized version of Rytova-Keldysh theory<sup>21</sup> developed by Muljarov et al.<sup>32</sup> and Guseinov.<sup>34</sup> As shown in Figure 3H, the known E<sub>b</sub> values fall between the binding energies calculated using  $\varepsilon_{\infty}$  and  $\varepsilon_{0}$  separately, which suggests that the relevant screening frequency is between those two limits; i.e., that the electron-hole interaction is partially screened by phonons. A similar argument in favor of phonon screening is found by returning to the question of  $\gamma$ ; i.e., the extent to which excitons in 2D HPs deviate from the Wannier model because of dielectric and quantum confinement effects. As detailed in Note S13, we calculate  $2.4 < \gamma < 3.2$  for any reasonable combination of dielectric constants, and this range falls inside the  $\gamma$  = 1.83 and  $\gamma$  = 8.44 bounds that were measured using  $\varepsilon_{\infty}$  and  $\varepsilon_{0}$ , respectively, hence implying a certain degree of phonon screening. The statistical significance of the disagreement between experiment and theory using  $\varepsilon_{\infty}$  ranges from  $0.9\sigma$ – $5.1\sigma$ for the 19 structures that were studied (Note \$14). Because of the success of the Rytoka-Keldysh potential in other contexts<sup>2,35</sup> and the fact that Bethe-Salpeter approaches also overpredict  $E_b$  in 2D HPs when using  $\varepsilon_{\infty}$ ,  $^{4,36-38}$  we interpret this disagreement not as an indictment of the theory but, rather, as a strong indicator that phonons partially screen the electron-hole interaction.

These calculations reveal that the actual dielectric constant responsible for the exciton screening lies between the bounds set by  $\varepsilon_{\infty}$  and  $\varepsilon_0$ . To determine the value of this effective dielectric constant ( $\varepsilon'$ ), we fit a theoretical  $E_b$  vs.  $I_b$  curve to our experimental measurements. In Figure 4D, we plot  $E_b$  as a function of  $I_b$  using multiple members of the  $(C_m)_2$ PbI<sub>4</sub> series, with  $I_b$  being determined by XRD patterns (Figure 4A) and  $E_b$  being determined from absorption (Figure 4B) and EA spectra (Figure 4C; details in Note S4). As mentioned previously, leading models classify 2D HPs as isolated quantum wells and, hence, assume that  $E_b$  is independent of  $I_b$ .<sup>21</sup> However, the gradual rise in  $E_b$  moving from (C<sub>4</sub>)<sub>2</sub>PbI<sub>4</sub> to (C<sub>16</sub>)<sub>2</sub>PbI<sub>4</sub> (Figure 4D) demonstrates otherwise and shows that there is communication between wells;  $E_b$  is lower when  $I_b$  is small because an exciton in a [Pbl<sub>4</sub>]<sup>2-</sup> sheet is partially screened by neighboring inorganic sheets. The theoretical model based on a superlattice of quantum wells captures this effect (black line), where the curvature of  $E_b$  vs.  $I_b$  is very sensitive to the ratio  $\varepsilon_w/\varepsilon_b$ , and the vertical offset is extremely sensitive to the overall magnitude of the dielectric constants. Using the average phase II mass obtained from DFT ( $\mu = 0.140m_0$ ), we performed a least-squares fit to obtain  $\varepsilon_w' = 6.15$  and  $\varepsilon_b' = 2.8$  (Figure 4D, black line). At this level of theory, the agreement with experiments is excellent. Not only are the small deviations between the fit line and individual  $(C_m)_2$ PbI<sub>4</sub> members accurately captured changes in  $\mu$  that are a result of octahedral tilting (Figure 4D, asterisks), but additionally, repeating the calculation using the phase I mass obtained from DFT,  $\mu = 0.111 m_0$ , produces an  $E_b$  vs.  $I_b$  curve in near-perfect agreement with our  $E_b$  measurements on phase I structures (Figure 4D red line).

For materials in which  $E_b/\hbar$  is closer to  $\omega_{LO}$ , the time scales of phonon and exciton motion become more closely matched, and the phonon screening is expected to become more efficient.<sup>27,39</sup> Therefore, the phonon screening efficiency ( $\alpha$ ) and  $E_b$  share an inverse relationship, and indeed, we observe a slight inverse relationship for the 20 structures where  $\alpha$  was obtained (Figure \$16). Therefore, we expect



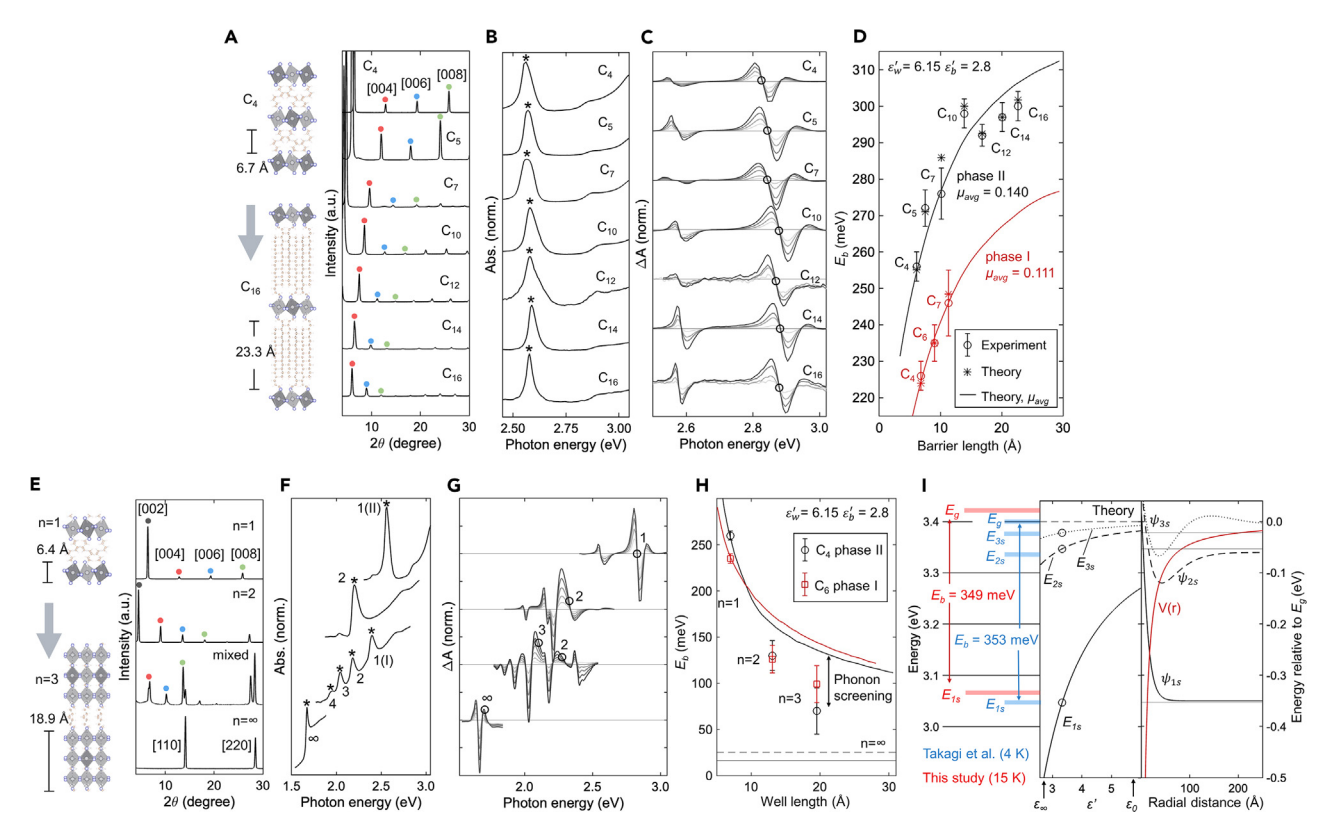


Figure 4. Comparison of theory vs. experiment

- (A) XRD patterns of  $(C_m)_2$ PbI<sub>4</sub> structures showing a monotonic decrease in the 2 $\theta$  separation between  $\{00l\}$  peaks as carbon atoms are incorporated into the alkyl chain.
- (B) Absorption spectra of multiple  $(C_m)_2 PbI_4$  structures, where  $E_{1s}$  is marked by an asterisk.
- (C) The corresponding EA spectra, where  $E_g$  is marked by an open circle.
- (D) The relationship between  $E_b$  and  $I_b$ . Error bars denote one standard deviation. The data point for  $(C_6)_2$ PbI $_4$  was acquired by our interpretation of the EA spectrum published by Tanaka and Kondo.
- (E) The crystal structures and XRD patterns for the  $BA_2MA_{n-1}Pb_nI_{3n+1}$  series, where n represents the number of lead-iodide octahedral layers within the well
- (F and G) Absorption spectra of the n = 1, n = 2, n =  $\{1,2,3,4\}$  (mixed), and n =  $\infty$  thin films (F) and corresponding (G) EA spectra.
- (H) The relationship between  $E_b$  and  $I_{w}$ , where the data points for the  $(C_6)_2MA_{n-1}Pb_nI_{3n+1}$  were acquired by our interpretation of the EA spectrum published by Tanaka and Kondo. <sup>40</sup> Error bars denote one standard deviation.
- (I) Left: our  $E_g$  and  $E_{1s}$  assignments for PEA<sub>2</sub>PbBr<sub>4</sub> in comparison with those made by Takagi et al., <sup>42</sup> where  $E_{2s}$  and  $E_{3s}$  were also determined. Center: our theoretical calculation of  $E_{1s}$ ,  $E_{2s}$ , and  $E_{3s}$  as a function of the effective dielectric constant ( $\epsilon'$ ); the theory and experiment agree best when  $\epsilon' = 3.33$ . Right: the Coulomb potential as a function of electron-hole separation (V(r); red line) and the computed wavefunctions for the 1s, 2s, and 3s exciton states.

nominal  $E_b$ -lowering alterations to the 2D HP structure to be doubly effective at lowering  $E_b$ . For example,  $E_b$  and  $I_w$  share an inverse relationship in any quantum-confined system; however, we expect the relationship to be even more pronounced in HPs, where the nominal reduction of  $E_b$  with  $I_w$  is accompanied by an increase in phonon screening. To test this hypothesis, we compare experimentally determined  $E_b$  vs.  $I_w$  curves against the model predictions using a set of samples prepared with the same barrier molecule (BA) but varying the number of inorganic octahedral layers (n) within the  $BA_2MA_{n-1}Pb_nI_{3n+1}$  formula. The XRD, absorption, and EA of n=1, n=2,  $n=\{1,2,3,4\}$  (mixed), and  $n=\infty$  structures are shown in Figures 4E–4G. The XRD provides information on  $I_w$ , while the absorption and EA yield the  $E_{1s}$  and  $E_g$  energies, respectively. Our assignments of the latter two parameters for n>1 structures were informed by simulations of a 3D Wannier exciton in an electric field (Note \$16). The resulting  $E_b$  vs.  $I_w$  relationship is shown in Figure 4H



alongside that of  $(C_6)_2MA_{n-1}Pb_nI_{3n+1}$ , where our analysis of EA spectra reported by Tanaka and Kondo<sup>40</sup> produced the data points for n = 1, n = 2, and n = 3 C<sub>6</sub> structures (Figure S29). Our measurements of the material parameters reveal three primary reasons why  $E_b$  decreases when moving from 2D  $\rightarrow$  3D: (1) an increase in  $I_w$ , (2) a slight decrease in  $\mu$ , and (3) a moderate increase in  $\varepsilon_0$  because the phonons in the 3D network are more polarizable. Because each of these serves to reduce  $E_b$ , we expect an accompanying secondary effect of (4) increased phonon-screening efficiency which further reduces  $E_b$ . The combination of these four effects produces the extremely low value of  $E_{b,3D}$  = 16 meV<sup>41</sup> for MAPbI<sub>3</sub>. The superlattice model in the limit that  $l_w$  becomes large and  $\mu$  decreases to its 3D value of 0.104  ${\rm m_0}^{41}$  accounts for effects (1) and (2) but not (3) and (4). Hence, we attribute the discrepancy between theory and experiment shown in Figure 4H to increased phonon screening at large  $I_w$ . These myriad factors moving from 2D  $\rightarrow$  3D make the relationship between  $E_b$  and  $I_w$  more complicated than previously proposed quantum confinement models based on fractional dimensionality. The dependencies of  $E_b$  on the other material parameters ( $\varepsilon_w$ ,  $\varepsilon_b$ , and  $\mu$ ) are not as clearly resolved experimentally as those shown here for  $l_w$  and  $l_b$ , but we find that the model agrees with experiments to the extent that we measure these relationships (Figure S22).

For our final test of the superlattice model, we investigate the exciton's Rydberg energy ladder because the FK feature near 2.8 eV for BA<sub>2</sub>PbI<sub>4</sub> (Figure 1) challenges the previous measurements of  $E_g$  = 3 eV based on believed Rydberg features<sup>4,7</sup> and opens the question of whether higher Rydberg members (2s, 3s, etc.) have ever been observed in 2D HPs. Br-based compounds offer the best opportunity to resolve such states in absorption experiments because of the confluence of high crystallinity and enhanced exciton absorption strength. Figure 4I shows that our  $E_{1s}$  and  $E_g$  measurements for PEA<sub>2</sub>PbBr<sub>4</sub> agree with a study by Takagi et al.,<sup>42</sup> where  $E_g$  was inferred from reproducible measurements of  $E_{2s}$  and  $E_{3s}$ . As shown in Figure 4K, when an effective dielectric constant  $\varepsilon'_{bulk}$  = 3.33 is used (between  $\varepsilon_{\infty}$  = 2.74 and  $\varepsilon_0$  = 5.86), the theoretical model predicts 1s, 2s, and 3s energies in alignment with experiments (Figure 4I, center), and with radial wavefunctions (Figure 4I, right).

With this enhanced understanding of excitons in 2D HPs, we can return to the question of the peculiar  $E_g$ - $E_b$  correlation observed in Figure 2B; namely, why does the experimental trend of  $E_b = 0.180E_a - 0.249$  deviate from the theoretically predicted trendline of  $E_b = 0.25E_g$ ? Specifically, the results in Figure 4 demonstrate the significance of superlattice screening and phonon screening in 2D HPs, and these insights reveal that 2D HPs violate certain assumptions inherent to the  $E_b = 0.25E_a$  trendline, such as the assumption that the well layer is suspended in an infinite vacuum and the assumption that excitons are screened only by the optical dielectric constant. However, one can conceive a hypothetical 2D-HP-related system where these assumptions are honored, such as a freestanding  $[BX_4]^{2-}$  sheet where phonons do not contribute to the exciton screening. The excitonic properties of this system can be calculated using the superlattice model in the limit  $l_b \to \infty$ ,  $\varepsilon_b \to 1$ , and  $\varepsilon_w \to \varepsilon_{w,\infty}$ , and, as shown in Figure 5A, doing so produces  $\{E_a, E_b\}$  values that follow the  $E_b = 0.25E_a$  trendline (see details in Note S7). Thus, these additional screening sources (superlattice screening  $l_b < \infty$ , barrier screening  $\varepsilon_b > 1$ , and phonon screening  $\varepsilon_w > \varepsilon_{w,\infty}$ ) serve to lower  $E_b$  in real 2D HPs, and this results in the experimentally observed trendline with a lower slope and negative y axis intercept.

The  $\{E_g, E_b\}$  values of PEA- and BA-based 2D HPs fall almost exactly on a common linear slope (Figure 5A). This, coupled with the fact that 2D HPs deviate significantly from the ideal 2D systems conceptualized for the  $E_b = 0.25E_g$  trendline, suggests





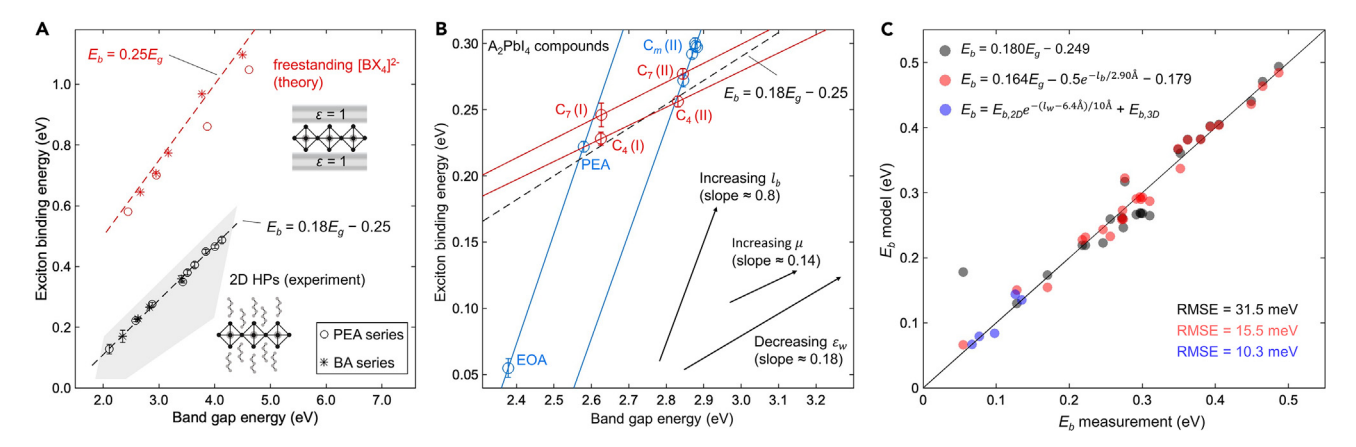


Figure 5.  $E_g$ - $E_b$  engineering

(A)  $E_b$  vs.  $E_g$  relationship for PEA- and BA-based 2D HPs as measured by EA (black) in comparison with freestanding  $[BX_4]^{2-}$  monolayers suspended in a vacuum, as calculated by the superlattice model. The shaded area is our estimate for the total  $\{E_g, E_b\}$  parameter space accessible through known chemical substitutions.

(B) The  $E_b$  vs.  $E_g$  for various  $A_2PbI_4$  compounds, which reveals the effects of  $I_b$  and  $\mu$  on  $E_g$  and  $E_b$ . The effect of  $\varepsilon_w$  is shown as a dotted black line, which was obtained by fitting to the  $PEA_2BX_4$  series in (A).

(C) The accuracy of predicting  $E_b$  for n = 1 HPs simply from  $E_g$  (black) and  $E_g$  and  $I_b$  (red) as well as the accuracy of predicting  $E_b$  for n > 1 HPs from knowledge of the  $E_{b,2D}$ ,  $E_{b,3D}$ , and  $I_w$  (blue).

that  $E_g$ - $E_b$  correlations are stronger and more universal than currently realized. Because the dielectric constant plays a dominant role in determining  $E_g$  and  $E_b$  in low-dimensional systems,  $^{43-45}$  similarly strong  $E_g$ - $E_b$  correlations almost certainly exist in other 2D semiconductors, such as monolayer TMDCs, II-VI quantum wells, III-V quantum wells, etc., and also very likely exist in 1D quantum wire and 0D quantum dot systems. In 3D systems,  $\mu$  plays a larger role in determining  $E_b$ , but strong correlations are still likely due to the relationship between  $\mu$  and  $E_g$  in 3D systems. Indeed, a global correlation between  $E_g$  and  $E_b$  has been noticed in previous studies by compiling separate measurements on 3D semiconductors. However, the strength of the correlation is largely unknown because of variance in measurement methodologies, and the nature of the correlation is debated. However, the small correlation of  $E_b = 0.0334E_g - 0.0406$  for 3D HPs, in accordance with previous studies,  $^{47,48}$  which results from both parameters  $\mu$  and  $\varepsilon$  evolving in a manner to increase  $E_b$  moving from MASnI<sub>3</sub>  $\rightarrow$  MAPbI<sub>3</sub>  $\rightarrow$  MAPbBr<sub>3</sub>  $\rightarrow$  MAPbCl<sub>3</sub> (Note S16).

Precise and accurate measurements of  $E_b$  and  $E_g$  are the bottleneck for determining which classes of semiconductors exhibit strong  $E_g$ - $E_b$  correlations. The large variance of  $E_b$  measurements currently in the literature <sup>10</sup> leaves much room for the possibility that strong  $E_g$  vs.  $E_b$  correlations are commonplace across many classes of semiconductors. The measurement method introduced in Figure 1 is ideal for measuring  $E_g$  and  $E_b$  in low-dimensional systems, where  $E_b$  is greater than the absorption broadening, and it can be implemented to search for  $E_g$ - $E_b$  correlations in other low-dimensional semiconductors.

Mapping the  $E_g$ - $E_b$  correlation is a great boon for the optimization and engineering of a given material system. Not only does it establish the  $\{E_g, E_b\}$  parameter space accessible through chemical alterations, but it also provides a roadmap for navigating this space. For the case of 2D HPs, the gray-shaded region in Figure 5A marks our estimate for the total range of  $\{E_g, E_b\}$  available, where the boundaries are set by understanding the effects of known chemical substitutions. For example, the primary change moving from  $C_4 \rightarrow C_{16}$  (and also for EOA  $\rightarrow$  PEA) is an increase in  $I_b$ , and the



 $\{E_g, E_b\}$  points of these structures follow lines with slope  $\approx 0.8$  (Figure 5B). The lower (upper) limit of  $I_b$  in 2D HPs is roughly set by EOA ( $C_{16}$ ), with  $I_b = 3.65$  Å (23.25 Å). The PEA<sub>2</sub>BX<sub>4</sub> series reveals that a decrease in  $\varepsilon_w$  allows tunability along lines with a shallower slope of 0.18, where the lower (upper) limit is set by  $[SnI_4]^{2-}$  ( $[PbCI_4]^{2-}$ ) with  $\varepsilon_{w,\infty} = 4.95$  (2.79). An even shallower slope of 0.14 is observed moving from phase I to phase II versions of  $C_4$  and  $C_7$ , where the primary change in both cases is an increase of  $\mu$  from  $\sim$ 0.11 to  $\sim$ 0.14  $m_0$ . In addition to these valuable insights, the  $E_g$ - $E_b$  correlation can also be leveraged to accurately predict  $E_g$  and  $E_b$  of materials not included in the dataset. In the case of 2D HPs, the global linear fit of  $E_b = 0.180E_g - 0.249$  (model 1) is one example, and this can be improved by a two-parameter empirical model that accounts for the more vertical tunability in terms of barrier length ( $I_b$ ):  $E_b = 0.164E_g - 0.5$  e<sup>- $I_b/2.90Å$ </sup> – 0.179 (model 2), where the energies are in units of eV and lengths in units of angstrom.

The accuracies of these two models are presented in Figure 5C, and the root-meansquare (RMS) errors of 31 and 16 meV, respectively, are far smaller than experimental errors associated with common Eb measurement techniques. To predict  $E_b$  for n > 1 HPs, we again opt for a phenomenological model; namely an exponential decay connecting the known  $E_{b,2D}$  (n = 1) and  $E_{b,3D}$  (n =  $\infty$ ) values as follows:  $E_b(l_w)=E_{b,2D}~{\rm e}^{-(l_w-6.4 {\rm \AA})/10 {\rm \AA}}+E_{b,3D},$  where  $E_{b,2D}$  is the model 2 equation and  $E_{b,3D} = 0.0334E_g - 0.0406$  (Note S16). Upon substituting  $E_g = E_{1s} + E_b$  and  $l_b = d_{002} - l_w$ , where  $d_{002}$  is the interlayer spacing and  $l_w = n(6.4 \text{ Å})$ , a highly accurate ( $\pm$ 16 meV) prediction of  $E_b$  can be obtained for any HP system using two simple pieces of experimental information,  $E_{1s}$  and  $d_{002}$ , which can be determined from room temperature optical absorption (or PL) and XRD, respectively.<sup>50</sup> Thus, the  $E_q$ - $E_b$  correlation is a powerful tool for device engineering, especially considering that  $E_b$  is a strong correlate with other important properties, such as absorption strength, PL quantum yield, exciton radius, exciton lifetime, etc. When band-gap engineering is utilized to select the optimal value of  $E_{q}$ , it is helpful to recognize that this selection cannot take place independent of these other excitonic properties for 2D systems. Photovoltaic and photodetector devices generally require low  $E_b$  (tens of meVs) to promote exciton disassociation, while  $E_a$  generally falls in the range of 1.1–1.5 eV for photovoltaics, and  $E_a$  varies for photodetectors depending on the spectral range of interest. 51 For light-emitting applications, large  $E_b$  values are generally more favorable for increased electron-hole wavefunction overlap and higher recombination rates. As shown here for the case of 2D HPs, mapping the  $E_q$ - $E_b$  correlation allows one to predict  $E_q$  and  $E_b$  from simple experiments, and the optimal value of  $\{E_g, E_b\}$  can be selected for the application in question.

#### Conclusion

In summary, we have shown that essentially any HP system with  $E_b > 25$  meV is capable of producing a clear FK feature in its low-temperature EA spectrum and that analysis of this feature is the key to unlocking long-sought-after  $E_b$  values that are precise and trustworthy. This method was used to measure  $E_g$  and  $E_b$  values for 31 HP compounds (Table 1) and show that  $E_b$  is largely unaffected by morphology and temperature but, instead, is a robust property intrinsic to a given HP structure and highly tunable through chemical substitutions that alter the dielectric environment. When comparing the theoretical  $E_b$  calculations against a wide range of measurements ( $E_b$  vs.  $I_b$ ,  $E_b$  vs.  $I_w$ , and the exciton's Rydberg energy ladder), we conclude that calculations based on  $\varepsilon_\infty$  values overpredict  $E_b$ , which implies that electron-hole interactions are partially screened by phonons in 2D and 3D HPs. However, effective dielectric constants that include a portion of phonon screening bring the theory and experiment into harmony. Considering that  $E_b/\hbar$  is two orders of magnitude larger





than  $\omega_{LO}$  in 2D HPs, this result challenges the typical assumption that polarization mechanisms slower than  $(E_b/\hbar)^{-1}$  do not screen the electron-hole interaction  $^{26,27}$  and has wide implications for systems beyond HPs. Further theoretical work is needed to determine whether this strong phonon screening is specific to highly anharmonic systems such as HPs or general for all materials. Additional screening sources in 2D HPs, such as this phonon screening, are the key to understanding why the  $E_g$ - $E_b$  correlation in 2D HPs deviates from recent theoretical predictions. Despite these deviations, the measured  $E_g$ - $E_b$  is strikingly strong, and similarly strong  $E_g$ - $E_b$  correlations likely exist in other low-dimensional semiconductors because of the strong mutual dependence of  $E_g$  and  $E_b$  on the semiconductor's dielectric constant. By mapping the  $\{E_g, E_b\}$  parameter space and developing formulas to predict  $E_g$  and  $E_b$  from simple experiments, we demonstrate that there is much to gain by replacing the current field of band-gap engineering with the even more useful and technically accurate field of  $E_g$ - $E_b$  engineering.

#### **EXPERIMENTAL PROCEDURES**

#### Resource availability

#### Lead contact

Further information and requests for resources should be directed to and will be fulfilled by the lead contact, Kameron R. Hansen (kameron.hansen@utah.edu).

#### Materials availability

This study did not generate new unique reagents.

#### Data and code availability

All data reported in this paper will be shared by the lead contact upon request. All original code is publicly available as of the date of publication via Zenodo: https://doi.org/10.5281/zenodo.8075786.1. Any additional information required to reanalyze the data reported in this paper is available from the lead contact upon request.

#### **Materials**

The following materials were purchased and used in this study without modification: 2-pentafluorophenylacetonitrile (99%, Aldrich), 2-phenylethylamine hydrochloride (PEACI; ≥98%, Aldrich), TEA (96%, Aldrich), acetone (ASTM grade, Cole-Parmer), amylamine (C<sub>5</sub>; 99%, Aldrich), borane tetrahydrofuran complex solution (BH<sub>3</sub>-THF; Aldrich), butylamine (BA or C<sub>4</sub>; 99.5%, Aldrich), decylamine (C<sub>10</sub>; 95%, Aldrich), diethyl ether (Sigma), dimethyl sulfoxide (DMSO; ≥99.7%, Fisher), dodecylammine ( $C_{12}$ ; 98%, Aldrich), EOA ( $\geq$  98%, Aldrich), heptylamine ( $C_7$ ; 99%, Aldrich), hexadecylamine (C<sub>16</sub>; 98%, Aldrich), hexamethylenediamine (98%, Aldrich), hydriodic acid (HI;  $\geq$  57%, Aldrich), hypophosphorous acid (H<sub>3</sub>PO<sub>2</sub>; 50 wt % in H<sub>2</sub>O, Aldrich), isopropanol (IPA; ACS grade, Cole-Parmer), lead(II) bromide (PbBr<sub>2</sub>; 99.998%, Alfa Aesar), lead(II) chloride (PbCl<sub>2</sub>; 99.999%, Alfa Aesar), lead(II) iodide (PbI<sub>2</sub>; 99.999%, Aldrich), MA bromide (MABr; 99.99%, GreatCell Solar), MA chloride (MACI; 99.99%, GreatCell Solar), MA iodide (MAI; 99.99%, GreatCell Solar), n-BA bromide (BABr; ≥98%, Aldrich), n-BA iodide (BAI; >99%, GreatCell Solar), phenethylamine hydrobromide (PEABr; ≥98%, Aldrich), tetradecylamine (C<sub>14</sub>; 95%, Aldrich), tetrahydrofuran (THF; ≥99.9%, Aldrich), tin(II) bromide (SnBr<sub>2</sub>; Aldrich), tin(II) fluoride (SnF<sub>2</sub>; 99%, Aldrich), and tin(II) iodide (SnI<sub>2</sub>; 99.99%, Aldrich).

#### **HP** sample preparation

We synthesized single crystal flakes for the following materials:  $BA_2PbI_4$ ,  $BA_2MAPb_2I_7$ ,  $BA_2MA_2Pb_3I_{10}$ ,  $TEA_2PbI_4$ ,  $EOA_2PbI_4$ ,  $HDAPbI_4$ ,  $(C_5)_2PbI_4$ ,  $(C_7)_2PbI_4$ ,  $(C_{10})_2PbI_4$ ,  $(C_{12})_2PbI_4$ ,  $(C_{14})_2PbI_4$ , and  $(C_{16})_2PbI_4$  according to the "slow cooling in





HI" method. In brief, 2.232 g (10 mmol) of PbO was dissolved in a glass vial containing 10 mL of HI and 1.7 mL of  $H_3PO_2$ , and the solution was brought to a temperature that was near boiling (T  $\sim$  90°C). For the n = 2 and n = 3 compounds, a stoichiometric amount (5 mmol for n = 2, 6.67 mmol for n = 3) of MACI was then added and allowed to dissolve under high heat. Next, a stoichiometric amount (10 mmol for n = 1, 7 mmol for n = 2, 3.33 mmol for n = 3) of the organic amine was mixed in a vial containing 5 mL HI and allowed to cool in an ice bath. The two solutions were then mixed and brought to near boiling until all precursors were dissolved, resulting in a transparent yellow solution. Next, then solution was allowed to cool to room temperature, which resulted in precipitation of single crystal flakes. For millimeter-sized single crystals of BA<sub>2</sub>PbI<sub>4</sub>, used in some optical spectroscopy measurements, the solution was cooled to a point where crystals began to precipitate ( $\sim$ 80°C), left unperturbed for 3 days, and then slowly cooled an at average rate of 2°C/h to room temperature. All crystals were washed three times with diethyl ether, dried under a vacuum at 60°C overnight, and then placed in a glovebox for storage. An ammonium salt of 5F-PEA iodide was also synthesized by dissolving 5 g (24.1 mmol) of 2-pentafluorophenylacetonitrile in 80 mL of THF, slowly adding 84 mL of BH<sub>3</sub>-THF at 0°C, and then allowing the reaction to reflux overnight. After cooling to room temperature, 17 mL of HI was added, the solution was mixed for 1 h, 350 mL of ether was added, and then the solution was cooled to 0°C. The precipitated crystals were protected from light and dried in a vacuum, yielding 3.52 g (69% yield) of white crystals, which were confirmed to be 5F-PEA using proton nuclear magnetic resonance.

The thin films were fabricated in a glovebox by spin-coating a precursor solution with a low molarity (0.05–0.3 M) to target thin films with a peak optical density between 1 and 2. In the case of BA<sub>2</sub>PbI<sub>4</sub>, BA<sub>2</sub>MAPb<sub>2</sub>I<sub>7</sub>, BA<sub>2</sub>MA<sub>2</sub>Pb<sub>3</sub>I<sub>10</sub>, TEA<sub>2</sub>PbI<sub>4</sub>, EOA<sub>2</sub>PbI<sub>4</sub>,  $(C_5)_2 Pbl_4$ ,  $(C_7)_2 Pbl_4$ ,  $(C_{10})_2 Pbl_4$ ,  $(C_{12})_2 Pbl_4$ ,  $(C_{14})_2 Pbl_4$ , and  $(C_{16})_2 Pbl_4$ , the precursor solution was made by dissolving single crystal flakes in a 4:1 DMF:DMSO solvent mixture. For BA<sub>2</sub>SnI<sub>4</sub>, BA<sub>2</sub>PbBr<sub>4</sub>, PEA<sub>2</sub>SnI<sub>4</sub>, PEA<sub>2</sub>PbI<sub>4</sub>, PEA<sub>2</sub>SnBr<sub>4</sub>, PEA<sub>2</sub>PbBr<sub>x</sub>CI<sub>4-x</sub> with  $x = \{0, 1, 2, 2.66, 3.33, 4\}$ ,  $5F-PEA_2PbI_4$ , MAPbI<sub>3</sub>, MAPbBr<sub>3</sub>, and MAPbCl<sub>3</sub>, a stoichiometric ratio (2:1) of ammonium salts (e.g., A-X, where A = BA, PEA, etc. and X = Cl, Br, or I) and metal-iodide salts (e.g.,  $SnX_2$  or  $PbX_2$ ) was dissolved in a 4:1 DMF:DMSO solvent mixture. For PEAX<sub>2</sub>, where  $X = \{Br, Cl\}$ , the ammonium salt was first baked overnight in a vacuum at 65°C to remove possible H<sub>2</sub>O. For PEA<sub>2</sub>Sn<sub>4</sub> and BA<sub>2</sub>SnI<sub>4</sub>, a quarter-stoichiometric quantity of SnF<sub>2</sub> was added to the precursor solution to increase sample resistivity and reduce the oxidation of Sn<sup>2+</sup> to Sn<sup>4+</sup>. The resulting precursor solutions were stirred for 30 min at room temperature. To spin-coat a thin film, substrates were cleaned via sequential steps of sonication in soapy water, distilled water, acetone, and IPA, and then plasma cleaned under vacuum. The substrate material was soda-lime glass for all measurements except EA, impedance spectroscopy, and, in some cases, XRD, in which case a quartz substrate with an ~120-nm-thick gold layer of interdigitated fingers was used (Figure 3B). The precursor solution was pipetted onto the glass substrate and then spun at 4,000 rpm for 30 s to target film thicknesses between 80 and 300 nm for all films except those used in impedance spectroscopy. The spin speed was reduced (1,250-3,000 rpm), and the precursor solution molarity was increased significantly (0.2-1.2 M) for films used in impedance spectroscopy to target thicknesses between 0.2 and 3  $\mu m$ . For 5F-PEA<sub>2</sub>PbI<sub>4</sub> and HDAPbI<sub>4</sub>, the substrate and the precursor solution were preheated on a 160°C and 60°C hot plate, respectively, according to the hot cast method. After spin-coating, films were annealed for 10 min on a 100°C hot plate. The 2D HP compounds with A = {PEA, BA,  $C_5$ , 5F-PEA, HDA, EOA}, B = Pb, and X = {I, Br} formed films with high crystallinity and strong exciton absorption and therefore required a lower molarity (0.05-0.1 M), whereas a higher molarity (0.1-0.3 M) was needed for





all other compounds. For EOA<sub>2</sub>PbI<sub>4</sub>, the film was solvent annealed. After annealing on a hot plate, the film was removed from the glovebox and enclosed in a Petri dish with  $\sim$ 2 mL of dH<sub>2</sub>O for 2 min; this caused the film to evolve from yellow to orange and exhibit XRD indicative of the EOA<sub>2</sub>PbI<sub>4</sub> structure (Figure S25).

#### Structural characterization

For each of the HP thin films, the structure and phase purity were determined by collecting XRD patterns using a Bruker D8 Discover X-ray diffractometer with Cu- $K\alpha$  radiation (Figure S25). The d<sub>002</sub> spacings were calculated using Bragg's law and verified to agree with SC-XRD reports in the literature (Table 1). For several of the thin films, atomic force microscopy (AFM) images were collected on a Bruker Dimension Icon atomic force microscope in tapping mode to determine the surface morphology (Figure S27). For the in-plane EA measurements, it is necessary for the quantum well layers to be parallel to the substrate because out-of-plane electric fields result in EA effects that are not accounted for in our simulation. 52 To determine the orientation of the quantum wells relative to the substrate and the electric field, we collected grazing-incidence wide-angle X-ray scattering (GIWAXS) images on beamline 11-3 at the Stanford Synchrotron Radiation Lightsource (Figure S24). A 12.7-keV X-ray beam was angled at 0.2° with respect to the substrate, which is below the substrate's critical angle and above the film's critical angle. The diffraction pattern was collected on a 3,072 × 3,072 pixel charge-coupled device (CCD) array positioned 315 mm from the sample. All images were background, polarization, and absorption corrected using the GIXSGUI software,<sup>53</sup> and distortion from the latter two effects was negligible. The homogeneity of the quantum well orientation parallel to the substrate was quantified from the φ dependence of the [002] peak (Figure S24), and the narrow distribution centered around  $\varphi = 0^{\circ}$  provided confidence in the EA signal's in-plane nature; i.e., with the electric field parallel to the quantum wells. The surface morphology and thickness of thin films used in EA and dielectric measurements were determined via optical profilometry. To measure the thickness, a scratch was made on the film surface to expose the substrate surface, and a 3D height scan was acquired over the scratched area.

#### **EA** and absorption spectroscopies

HP films were spin coated on an IDE array (Figure 3B) for absorbance and EA measurements. The small distance between opposing IDE fingers (45 μm) allowed generation of large electric fields parallel to the substate (11-155 kV/cm) and, by extension, parallel to the quantum well layers. The samples were mounted in a cryostat, and thin copper wires were soldered to the opposing electrode stripes. The output of a Xe lamp was spectrally filtered through a 0.25-m f/3.5 monochromator with typical 1.5-nm spectral resolution, focused on the sample, and then refocused on a UV-enhanced silicon photodiode detector. The RMS value of the photodiode's signal at a modulating frequency was detected using a Stanford Research Systems SR810 or SR830 lock-in amplifier. For each sample, the sample transmission (7), substrate transmission  $(T_0)$ , and sample electrotransmission  $(\Delta T)$  were collected as independent wavelength scans over the same range with the same step size. For T and  $T_0$ , the lockin was referenced to a mechanical chopper in the light beam (330 Hz, lockin referenced to the first harmonic). For  $\Delta T$ , the modulation was obtained via a specialized high-voltage pulse generator made by Lasermetrics/FastPulse Technology, which provided pulse wave voltages rising from 0 to (300–700 V) at a frequency of 983 Hz with a duty cycle close to 50%. Here, the lockin was again referenced to the first harmonic of the modulating signal,  $V_{AC}$ , unlike EA experiments done with sinusoidally varying voltages, which must be referenced to the second harmonic. The reported absorbance was calculated as  $A = -log_{10}(T/T_0)$ , and the EA response is then



given by  $\Delta A = -log_{10}(1 + \Delta T/T)$ .<sup>15</sup> The sign (+/-) of the EA signal was established from the quadratic Stark shift of the exciton, which manifests in the EA as positive first derivative lineshape.

#### **Dielectric spectroscopy**

Dielectric spectroscopy was performed on the samples at room temperature using an HP 4192A impedance analyzer. Short wires connected the analyzer's test fixture to the IDE electrodes. Capacitance values for IDE substrates with and without HP films were measured at 101 discrete frequencies from 5 Hz–13 MHz on a logarithmic scale. Eight averages were done on the lowest 30 points to eliminate noise, but samples with extremely low capacitance required 288 averages to sufficiently reduce noise. These measurements were done in parallel circuit mode to permit measurements of lower capacitance values than series mode allows. After the impedance measurements were collected, the heights of the HP films were measured using optical profilometry. The film thicknesses and capacitance values at different frequencies were then converted to the dielectric function  $\varepsilon(f)$  in accordance with the method outlined in Supplemental section 9.

#### Theoretical calculations

Experimentally determined structures were retrieved from the Cambridge Crystallographic Data Centre (CCDC) with d<sub>002</sub> spacings in agreement with the materials in this study (Table S4). We consider the retrieved structures to be the equilibrium structure and used these as a starting point for electronic structure and optical response calculations. All DFT calculations were performed with the generalized gradient approximation (GGA) proposed by Perdew et al.<sup>54</sup> (Perdew-Burke-Ernzerhof [PBE]) to describe the exchange-correlation functional implemented within the Vienna Ab-initio Simulation Package (VASP) code. 55,56 Sampling of the Brillouin zone used the k-points grids listed in Table S4. Single-particle wavefunctions were expanded into a plane-wave basis set with an energy cutoff of 600 eV for BA and PEA series and 700 eV for the (C<sub>m</sub>)<sub>2</sub>PbI<sub>4</sub> series. The convergence criterion for total energy was within 0.075-0.868 meV per atom. Static ( $\varepsilon_0$ ) and electronic ( $\varepsilon_\infty$ ) dielectric tensors at zero frequency are computed using density functional perturbation theory (DFPT) and independent quasiparticle approximation, respectively. 57,58 The diagonal components of the electronic dielectric tensor at zero frequency are computed, including a scissor shift determined by the difference between the PBE and the experimental band gap measured by EA. For PEA<sub>2</sub>PbI<sub>4</sub>, we verified that this result agrees with diagonal components of the dielectric tensor computed using the hybrid HSE06 functional<sup>59</sup> to describe exchange and correlation. Effective electron and hole mass tensors were calculated using the effective mass calculator (EMC)<sup>60</sup> at the conduction band minima and valence band maxima of the DFT-PBE band structure.

The electric field dependence of a Wannier exciton's absorption spectrum was calculated using in-house code written in MATLAB based on the theory of Dow and Redfield. The Numerov method was used to solve the Schrödinger equation for a Wannier exciton in an electric field and relate the solutions to the absorption through Elliott's equation (Note S1). The superlattice calculations based on the theory of Muljarov et al. and Guseinov were run using in-house code written in MATLAB and Mathematica (Note S12).

#### SUPPLEMENTAL INFORMATION

Supplemental information can be found online at https://doi.org/10.1016/j.matt. 2023.07.004.





#### **ACKNOWLEDGMENTS**

This work was supported by the US Department of Energy, Office of Basic Energy Sciences, Division of Materials Sciences and Engineering under award DE-SC0019041. K.R.H. acknowledges support from the National Science Foundation through a graduate research fellowship (grant 1747505). L.W.-B. acknowledges support from the Sloan Foundation through an Alfred P. Sloan Research Fellowship in Chemistry. C.Y.W. and A.S. acknowledge support from the National Science Foundation under grant 1922758. Support and resources from the Center for High Performance Computing at the University of Utah are acknowledged. This work made use of the Illinois Campus Cluster, a computing resource that is operated by the Illinois Campus Cluster Program (ICCP) in conjunction with the National Center for Supercomputing Applications (NCSA) and that is supported by funds from the University of Illinois at Urbana-Champaign. This work was performed in part at the Center for Integrated Nanotechnologies, an Office of Science User Facility operated for the US Department of Energy (DOE) Office of Science. Los Alamos National Laboratory, an affirmative action equal opportunity employer, is managed by Triad National Security, LLC for the US Department of Energy's NNSA under contract 89233218CNA000001. M.E. was supported by the NSF REU program, grant 2051129. C.E.M., B.R., D.J.K., and C.M.S. were supported in full or in part by the BYU Department of Physics and Astronomy and BYU College of Physical and Mathematical Sciences.

#### **AUTHOR CONTRIBUTIONS**

Conceptualization, K.R.H.; methodology, K.R.H.; investigation, K.R.H., C.Y.W., A.S., C.E.M., B.R., L.F., D.P., K.G., A.B., M.E., D.J.K., C.M.S., J.S.C., and L.W.-B.; writing – original draft, K.R.H.; writing – review & editing, K.R.H. and J.S.C.; funding acquisition, L.W.B., K.R.H., J.S.C., and A.S.; resources, L.W.B., J.S.C., and A.S.; supervision, L.W.B., J.S.C., M.C.B., and A.S.

#### **DECLARATION OF INTERESTS**

The authors declare no competing interests.

Received: March 29, 2023 Revised: June 11, 2023 Accepted: July 3, 2023 Published: July 28, 2023

#### **REFERENCES**

- Blancon, J.-C., Even, J., Stoumpos, C.C., Kanatzidis, M.G., and Mohite, A.D. (2020). Semiconductor physics of organic-inorganic 2D halide perovskites. Nat. Nanotechnol. 15, 969–985. https://doi.org/10.1038/s41565-020-00811-1.
- Wang, G., Chernikov, A., Glazov, M.M., Heinz, T.F., Marie, X., Amand, T., and Urbaszek, B. (2018). Colloquium: Excitons in atomically thin transition metal dichalcogenides. Rev. Mod. Phys. 90, 021001. https://doi.org/10.1103/ RevModPhys.90.021001.
- Hansen, K.R., Romrell, B., McClure, C.E., Eggleston, M., Berzansky, A., Lin, J.W., Garden, K., Whittaker-Brooks, L., and Colton, J.S. (2023). Ruddlesden-Popper Perovskite Alloys: Continuous and Discontinuous Tuning of the Electronic Structure. J. Phys. Chem. C

- 127, 9344–9353. https://doi.org/10.1021/acs.jpcc.3c01294.
- Blancon, J.C., Stier, A.V., Tsai, H., Nie, W., Stoumpos, C.C., Traoré, B., Pedesseau, L., Kepenekian, M., Katsutani, F., Noe, G.T., et al. (2018). Scaling law for excitons in 2D perovskite quantum wells. Nat. Commun. 9, 2254. https:// doi.org/10.1038/s41467-018-04659-x.
- Ziegler, J.D., Lin, K.-Q., Meisinger, B., Zhu, X., Kober-Czerny, M., Nayak, P.K., Vona, C., Taniguchi, T., Watanabe, K., Draxl, C., et al. (2022). Excitons at the Phase Transition of 2D Hybrid Perovskites. ACS Photonics 9, 3609–3616. https://doi.org/10.1021/acsphotonics. 2c01035.
- 6. Chen, X., Lu, H., Wang, K., Zhai, Y., Lunin, V., Sercel, P.C., and Beard, M.C. (2021). Tuning

- Spin-Polarized Lifetime in Two-Dimensional Metal-Halide Perovskite through Exciton Binding Energy. J. Am. Chem. Soc. 143, 19438–19445.
- Yaffe, O., Chernikov, A., Norman, Z.M., Zhong, Y., Velauthapillai, A., van der Zande, A., Owen, J.S., and Heinz, T.F. (2015). Excitons in ultrathin organic-inorganic perovskite crystals. Phys. Rev. B 92, 045414. https://doi.org/10.1103/ PhysRevB.92.045414.
- Ishihara, T. (1994). Optical properties of Pblbased perovskite structures. J. Lumin. 60–61, 269–274. https://doi.org/10.1016/0022-2313(94)90145-7.
- Chen, Z., Zhang, Q., Zhu, M., Wang, X., Wang, Q., Wee, A.T.S., Loh, K.P., Eda, G., and Xu, Q.H. (2020). Synthesis of Two-Dimensional



- Perovskite by Inverse Temperature Crystallization and Studies of Exciton States by Two-Photon Excitation Spectroscopy. Adv. Funct. Mater. 30, 2002661.
- Hansen, K.R., Colton, J.S., and Whittaker-Brooks, L. (2023). Exciton properties: learning from a decade of measurements on halide perovskites and transition metal dichalcogenides. Preprint at arXiv. https://doi. org/10.48550/arXiv.2306.14036.
- Lederman, F.L., and Dow, J.D. (1976). Theory of electroabsorption by anisotropic and layered semiconductors. I. Two-dimensional excitons in a uniform electric field. Phys. Rev. B 13, 1633–1642. https://doi.org/10.1103/PhysRevB. 13.1633.
- Dow, J.D., and Redfield, D. (1970).
   Electroabsorption in Semiconductors: The Excitonic Absorption Edge. Phys. Rev. B 1, 3358–3371. https://doi.org/10.1103/PhysRevB. 1,3358
- Hamakawa, Y., Germano, F.A., and Handler, P. (1968). Interband Electro-Optical Properties of Germanium. I. Electroabsorption. Phys. Rev. 167, 703–709. https://doi.org/10.1103/ PhysRev.167.703.
- Weiser, G., Horvath, A., and Kolbe, H. (1997). Franz-Keldysh effect of band states in polydiacetylene. Optical Probes of Conjugated Polymers, 3145. https://doi.org/10.1117/12. 279276.
- Hansen, K.R., McClure, C.E., Colton, J.S., and Whittaker-Brooks, L. (2022). Franz-Keldysh and Stark Effects in Two-Dimensional Metal Halide Perovskites. PRX Energy 1, 013001.
- Amerling, E., Hansen, K.R., and Whittaker-Brooks, L. (2021). Resolving buried optoelectronic features in metal halide perovskites via modulation spectroscopy studies. J. Mater. Chem. A Mater. 9, 23746–23764.
- Grancini, G., Srimath Kandada, A.R., Frost, J.M., Barker, A.J., De Bastiani, M., Gandini, M., Marras, S., Lanzani, G., Walsh, A., and Petrozza, A. (2015). Role of microstructure in the electron-hole interaction of hybrid lead halide perovskites. Nat. Photonics 9, 695–701. https:// doi.org/10.1038/nphoton.2015.151.
- Lei, Y., Li, Y., Lu, C., Yan, Q., Wu, Y., Babbe, F., Gong, H., Zhang, S., Zhou, J., Wang, R., et al. (2022). Perovskite superlattices with efficient carrier dynamics. Nature 608, 317–323.
- Billing, D.G., and Lemmerer, A. (2007). Synthesis, characterization and phase transitions in the inorganic-organic layered perovskite-type hybrids [(CnH2n+ 1NH3) 2Pbl4], n= 4, 5 and 6. Acta Crystallogr. B 63, 735–747.
- Aspnes, D.E. (1973). Third-derivative modulation spectroscopy with low-field electroreflectance. Surf. Sci. 37, 418–442.
- Katan, C., Mercier, N., and Even, J. (2019).
   Quantum and dielectric confinement effects in lower-dimensional hybrid perovskite semiconductors. Chem. Rev. 119, 3140–3192.
- Cheng, B., Li, T.-Y., Maity, P., Wei, P.-C., Nordlund, D., Ho, K.-T., Lien, D.-H., Lin, C.-H., Liang, R.-Z., Miao, X., et al. (2018). Extremely reduced dielectric confinement in two-

- dimensional hybrid perovskites with large polar organics. Commun. Phys. 1, 80. https://doi.org/10.1038/s42005-018-0082-8.
- Lin, J.-T., Liao, C.-C., Hsu, C.-S., Chen, D.-G., Chen, H.-M., Tsai, M.-K., Chou, P.-T., and Chiu, C.-W. (2019). Harnessing Dielectric Confinement on Tin Perovskites to Achieve Emission Quantum Yield up to 21. J. Am. Chem. Soc. 141, 10324–10330. https://doi.org/ 10.1021/jacs.9b03148.
- Shi, J., Gao, Y., Gao, X., Zhang, Y., Zhang, J., Jing, X., and Shao, M. (2019). Fluorinated Low-Dimensional Ruddlesden–Popper Perovskite Solar Cells with over 17% Power Conversion Efficiency and Improved Stability. Adv. Mater. 31, 1901673. https://doi.org/10.1002/adma. 201901673.
- Jiang, Z., Liu, Z., Li, Y., and Duan, W. (2017). Scaling universality between band gap and exciton binding energy of two-dimensional semiconductors. Phys. Rev. Lett. 118, 266401.
- 26. Knox, R.S. (1963). Theory of Excitons (Academic Press).
- Bechstedt, F. (2015). Many-body Approach to Electronic Excitations Concepts and Applications (Springer).
- Kang, J., and Wang, L.-W. (2017). Dynamic Disorder and Potential Fluctuation in Two-Dimensional Perovskite. J. Phys. Chem. Lett. 8, 3875–3880. https://doi.org/10.1021/acs.jpclett. 7b01501
- DeCrescent, R.A., Venkatesan, N.R., Dahlman, C.J., Kennard, R.M., Chabinyc, M.L., and Schuller, J.A. (2019). Optical Constants and Effective-Medium Origins of Large Optical Anisotropies in Layered Hybrid Organic/ Inorganic Perovskites. ACS Nano 13, 10745– 10753. https://doi.org/10.1021/acsnano. 9b05504.
- Keldysh, L. (1979). Coulomb interaction in thin semiconductor and semimetal films. Soviet Journal of Experimental and Theoretical Physics Letters 29, 658.
- Whittaker, D.M., and Elliott, R.J. (1988). Theory of magneto-exciton binding energy in realistic quantum well structures. Solid State Commun. 68, 1–5. https://doi.org/10.1016/0038-1098(88) 90233-5.
- Muljarov, E.A., Tikhodeev, S., Gippius, N., and Ishihara, T. (1995). Excitons in self-organized semiconductor/insulator superlattices: Pblbased perovskite compounds. Phys. Rev. B 51, 14370–14378.
- Leguy, A.M.A., Azarhoosh, P., Alonso, M.I., Campoy-Quiles, M., Weber, O.J., Yao, J., Bryant, D., Weller, M.T., Nelson, J., Walsh, A., et al. (2016). Experimental and theoretical optical properties of methylammonium lead halide perovskites. Nanoscale 8, 6317–6327. https://doi.org/10.1039/C5NR05435D.
- Guseinov, R.R. (1984). Coulomb Interaction and Excitons in a Superlattice. phys. stat. sol. 125, 237–243. https://doi.org/10.1002/pssb. 2221250128
- Stier, A.V., Wilson, N.P., Velizhanin, K.A., Kono, J., Xu, X., and Crooker, S.A. (2018).
   Magnetooptics of Exciton Rydberg States in a Monolayer Semiconductor. Phys. Rev. Lett.

- 120, 057405. https://doi.org/10.1103/ PhysRevLett.120.057405.
- Molina-Sánchez, A. (2018). Excitonic States in Semiconducting Two-Dimensional Perovskites. ACS Appl. Energy Mater. 1, 6361–6367. https://doi.org/10.1021/acsaem.8b01326.
- Cho, Y., and Berkelbach, T.C. (2019). Optical Properties of Layered Hybrid Organic– Inorganic Halide Perovskites: A Tight-Binding GW-BSE Study. J. Phys. Chem. Lett. 10, 6189–6196. https://doi.org/10.1021/acs.jpclett. 9b02491.
- Filip, M.R., Qiu, D.Y., Del Ben, M., and Neaton, J.B. (2022). Screening of Excitons by Organic Cations in Quasi-Two-Dimensional Organic– Inorganic Lead-Halide Perovskites. Nano Lett. 22, 4870–4878. https://doi.org/10.1021/acs. nanolett.2c01306.
- Filip, M.R., Haber, J.B., and Neaton, J.B. (2021). Phonon Screening of Excitons in Semiconductors: Halide Perovskites and Beyond. Phys. Rev. Lett. 127, 067401. https:// doi.org/10.1103/PhysRevLett.127.067401.
- Tanaka, K., and Kondo, T. (2003). Bandgap and exciton binding energies in lead-iodide-based natural quantum-well crystals. Sci. Technol. Adv. Mater. 4, 599–604.
- 41. Miyata, A., Mitioglu, A., Plochocka, P., Portugall, O., Wang, J.T.-W., Stranks, S.D., Snaith, H.J., and Nicholas, R.J. (2015). Direct measurement of the exciton binding energy and effective masses for charge carriers in organic–inorganic tri-halide perovskites. Nat. Phys. 11, 582–587.
- Takagi, H., Kunugita, H., and Ema, K. (2013). Influence of the image charge effect on excitonic energy structure in organic-inorganic multiple quantum well crystals. Phys. Rev. B 87, 125421. https://doi.org/10.1103/PhysRevB.87. 125421.
- Jiang, Q., Tong, J., Scheidt, R.A., Wang, X., Louks, A.E., Xian, Y., Tirawat, R., Palmstrom, A.F., Hautzinger, M.P., Harvey, S.P., et al. (2022). Compositional texture engineering for highly stable wide-bandgap perovskite solar cells. Science 378, 1295–1300. https://doi.org/ 10.1126/science.adf0194.
- Perebeinos, V., Tersoff, J., and Avouris, P. (2004). Scaling of Excitons in Carbon Nanotubes. Phys. Rev. Lett. 92, 257402. https://doi.org/10.1103/PhysRevLett.92.257402.
- Walsh, A.G., Vamivakas, A.N., Yin, Y., Cronin, S.B., Unlü, M.S., Goldberg, B.B., and Swan, A.K. (2007). Screening of Excitons in Single, Suspended Carbon Nanotubes. Nano Lett. 7, 1485–1488. https://doi.org/10.1021/ nl070193p.
- Haug, H., and Koch, S.W. (2009). Quantum Theory of the Optical and Electronic Properties of Semiconductors (World Scientific Publishing Company).
- Chen, X., Lu, H., Yang, Y., and Beard, M.C. (2018). Excitonic Effects in Methylammonium Lead Halide Perovskites. J. Phys. Chem. Lett. 9, 2595–2603. https://doi.org/10.1021/acs.jpclett. 8b00526.
- Baranowski, M., Plochocka, P., Su, R., Legrand, L., Barisien, T., Bernardot, F., Xiong, Q., Testelin, C., and Chamarro, M. (2020). Exciton





- binding energy and effective mass of CsPbCl3: a magneto-optical study. Photon. Res. *8*, A50–A55. https://doi.org/10.1364/PRJ.401872.
- Choi, J.-H., Cui, P., Lan, H., and Zhang, Z. (2015). Linear Scaling of the Exciton Binding Energy versus the Band Gap of Two-Dimensional Materials. Phys. Rev. Lett. 115, 066403. https://doi.org/10.1103/PhysRevLett. 115.066403.
- Hansen, K.R., McClure, C.E., Powell, D., Hsieh, H.C., Flannery, L., Garden, K., Miller, E.J., King, D.J., Sainio, S., Nordlund, D., et al. (2022). Low Exciton Binding Energies and Localized Exciton-Polaron States in 2D Tin Halide Perovskites. Adv. Opt. Mater. 10, 2102698.
- Powell, D., Hansen, K.R., Flannery, L., and Whittaker-Brooks, L. (2021). Traversing Excitonic and Ionic Landscapes: Reduced-Dimensionality-Inspired Design of Organometal Halide Semiconductors for Energy Applications. Acc. Chem. Res. 54, 4371–4382. https://doi.org/10.1021/acs. accounts.1c00492.
- Miller, D.A.B., Chemla, D.S., Damen, T.C., Gossard, A.C., Wiegmann, W., Wood, T.H., and Burrus, C.A. (1984). Band-Edge Electroabsorption in Quantum Well Structures: The Quantum-Confined Stark Effect. Phys. Rev. Lett. 53, 2173–2176. https://doi.org/10.1103/ PhysRevLett.53.2173.
- 53. Jiang, Z. (2015). GIXSGUI: a MATLAB toolbox for grazing-incidence X-ray scattering data

- visualization and reduction, and indexing of buried three-dimensional periodic nanostructured films. J. Appl. Crystallogr. 48, 917–926.
- Perdew, J.P., Burke, K., and Ernzerhof, M. (1996). Generalized Gradient Approximation Made Simple. Phys. Rev. Lett. 77, 3865–3868. https://doi.org/10.1103/PhysRevLett.77.3865.
- Kresse, G., and Furthmüller, J. (1996). Efficient iterative schemes for ab initio total-energy calculations using a plane-wave basis set. Phys. Rev. B 54, 11169–11186. https://doi.org/10. 1103/PhysRevB.54.11169.
- Kresse, G., and Joubert, D. (1999). From ultrasoft pseudopotentials to the projector augmented-wave method. Phys. Rev. B 59, 1758–1775. https://doi.org/10.1103/PhysRevB. 59.1758.
- Baroni, S., and Resta, R. (1986). Ab initio calculation of the macroscopic dielectric constant in silicon. Phys. Rev. B 33, 7017–7021. https://doi.org/10.1103/PhysRevB.33.7017.
- Gajdoš, M., Hummer, K., Kresse, G., Furthmüller, J., and Bechstedt, F. (2006). Linear optical properties in the projector-augmented wave methodology. Phys. Rev. B 73, 045112. https://doi.org/10.1103/PhysRevB.73.045112.
- Krukau, A.V., Vydrov, O.A., Izmaylov, A.F., and Scuseria, G.E. (2006). Influence of the exchange screening parameter on the performance of screened hybrid functionals. J. Chem. Phys.

- 125, 224106. https://doi.org/10.1063/1. 2404663.
- **60.** Fonari, A., and Sutton, C. (2015). Effective Mass Calculator for Semiconductors (GitHub).
- Batalioto, F., Duarte, A.R., Barbero, G., and Neto, A.M.F. (2010). Dielectric Dispersion of Water in the Frequency Range from 10 mHz to 30 MHz. J. Phys. Chem. B 114, 3467–3471. https://doi.org/10.1021/jp910114y.
- 62. Segelstein, D.J. (1981). The Complex Refractive Index of Water (University of Missouri–Kansas City).
- Krupka, J., Derzakowski, K., Tobar, M., Hartnett, J., and Geyer, R.G. (1999). Complex permittivity of some ultralow loss dielectric crystals at cryogenic temperatures. Meas. Sci. Technol. 10, 387–392. https://doi.org/10.1088/ 0957-0233/10/5/308.
- 64. Poglitsch, A., and Weber, D. (1987). Dynamic disorder in methylammoniumtrihalogenoplumbates (II) observed by millimeter-wave spectroscopy. J. Chem. Phys. 87, 6373–6378. https://doi.org/ 10.1063/1.453467.
- Bokdam, M., Sander, T., Stroppa, A., Picozzi, S., Sarma, D.D., Franchini, C., and Kresse, G. (2016). Role of Polar Phonons in the Photo Excited State of Metal Halide Perovskites. Sci. Rep. 6, 28618. https://doi.org/10.1038/ srep28618.